Journal of Materials Chemistry B

ROYAL SOCIETY OF CHEMISTRY

PAPER

View Article Online
View Journal | View Issue

Check for updates

Cite this: J. Mater. Chem. B, 2025, 13, 14101

Savinase-functionalised oxidative drug-loaded nanocarriers enhance the treatment of solid colorectal tumours in a 3D cell culture model

Anel G. Mun, [ab] Nuriya Nurlankyzy, [ab] Saule Kalmagambetova, [a] Aidos Baumuratov, [d] Dos Sarbassov, [ab] Vesselin N. Paunov *[e] and Agata N. Burska *[bc]

Colorectal cancer (CRC) mutations drive resistance and poor prognosis, underscoring the need for more effective therapies. The oxidative drug therapy combining arsenic trioxide (ATO) and D-vitamin C (D-VC) has demonstrated promising efficacy by targeting mitochondrial functions and depleting antioxidant defences to induce apoptosis in CRC cells. ATO and D-VC create a hostile environment for cancer cells by simultaneously targeting mitochondrial metabolism and redox homeostasis, reducing their ability to adapt and survive. This study evaluated the cytotoxic effects of ATO/D-VC in 2D cell cultures and 3D cell models, known as clusteroids, generated from CRC cell lines HCT116 and SW620. In the 2D cultures, the ATO/D-VC combination significantly reduced cell proliferation to 40–60% and viability to below 30% of control levels. In contrast, clusteroids showed a more limited response, with proliferation reduced to 60–80% and viability to 80–90%, highlighting the impact of the extracellular matrix (ECM) and cell–cell interactions in limiting drug diffusion within structured tumour microenvironments. To overcome these drug diffusion barriers, ATO and D-VC were individually encapsulated in poloxamer-stabilized shellac-based nanoparticles (NPs) surface functionalized with Savinase, a protease known to degrade ECM components. The cell viability and cell proliferation assays demonstrated that nanoparticle-mediated delivery significantly enhanced treatment efficacy in clusteroids. Dual treatment of Savinase-coated ATO and D-VC loaded NPs caused pronounced disruption of clusteroid morphology and substantially reduced both viability and proliferation to approximately 30–40% of untreated control levels. Compared to the free drug and uncoated nanoparticle formulations, the Savinase-functionalized nanoparticle formulation achieved nearly twice the reduction in viability and proliferation, indicating a marked improvement in therapeutic effect. Unloaded Savinase-coated nanoparticles showed minimal impact, underscoring their biocompatibility. This approach demonstrates the potential of protease-functionalized nanoparticles to enhance the oxidative drug delivery and efficacy in CRC tumours and could potentially allow targeting the therapeutic resistance in other solid tumours with dense ECM barriers.

Received 19th August 2025,
Accepted 27th September 2025

DOI: 10.1039/d5tb01882j

rsc.li/materials-b

Introduction

Arsenic trioxide (ATO) and the D-enantiomer of vitamin C (D-VC) are promising cancer therapies due to their ability to induce oxidative stress and selectively kill malignant cells.[1,2] ATO is well-known for treating acute promyelocytic leukaemia (APL)[3] and has shown effectiveness against various solid tumours, including pancreatic, lung, breast, head and neck, gastrointestinal, liver, colorectal cancers, and neuroblastoma.[4–6] It exerts anticancer effects by increasing the reactive oxygen species (ROS), causing mitochondrial dysfunction, cytochrome *c* release, and apoptosis. ATO also inhibits oncogenic pathways like PI3K/AKT/mTOR, suppressing tumour growth.[4,9,10] Ascorbic acid (vitamin C or VC) has demonstrated selective anticancer activity through its involvement in oxidative stress pathways.[7,8] Although it acts as an antioxidant at low micromolar levels, it becomes a pro-oxidant at high, millimolar concentrations, generating hydrogen peroxide (H_2O_2) that

[a] Department of Biology, School of Sciences and Humanities, Nazarbayev University, Astana, Kazakhstan
[b] National Laboratory Astana, Nazarbayev University, Astana, Kazakhstan. E-mail: agata.burska@nu.edu.kz
[c] Department of Biomedical Science, School of Medicine, Nazarbayev University, Astana, Kazakhstan
[d] Core Facilities, Nazarbayev University, Astana, Kazakhstan
[e] Department of Chemistry, School of Sciences and Humanities, Nazarbayev University, Astana, Kazakhstan. E-mail: vesselin.paunov@nu.edu.kz

selectively kills tumour cells.[11,12,14–16] VC also influences hypoxia-inducible factor (HIF) regulation and epigenetic mechanisms and impedes epithelial–mesenchymal transition (EMT) in cancers with KRAS or BRAF mutations by affecting glucose transporter expression, hence leading to higher dehydroascorbic acid (DHA) absorption and alteration of glycolytic pathways.[17–22] D-VC disrupts mitochondrial function and ATP production, sensitizing tumours to oxidative damage, and has a longer plasma half-life than L-VC.[2,23]

The combination of ATO and D-VC synergistically induces oxidative stress, depletes intracellular glutathione (the main antioxidant in the cell), and enhances ATO uptake, selectively killing KRAS-mutant cancer cells and overcoming drug resistance in colorectal cancer.[8,22,24,25] This combination targets mitochondrial metabolism and redox balance, creating an inhospitable environment for cancer cells. However, most evidence comes from 2D cultures and animal xenograft models,[2,23,24] limiting understanding of efficacy in complex tumour microenvironments.

In the present study, this drug combination was tested on a three-dimensional (3D) CRC cell model based on clusteroids. The cell clusteroid model provides a more accurate simulation of tumour complexity and drug response than traditional 2D cell cultures and has emerged as an essential tool in cancer research due to its improved ability to replicate the structural and functional characteristics of solid tumours typically observed *in vivo*. Unlike 2D monolayers, which do not capture spatial gradients of oxygen, nutrients, and signalling molecules, 3D models allow for the formation of hypoxic cores and support more realistic cell–cell and cell–matrix interactions.[47] These features are significant for evaluating drug responses and understanding resistance mechanisms in a tumour-like environment.[26–28] A widely adopted method for generating clusteroids involves the use of a water-in-water emulsion based on an aqueous two-phase system (ATPS) of dextran (DEX) and poly(ethylene oxide) (PEO).[26,29–31] The ATPS-based emulsion method rapidly generates biocompatible and scalable 3D clusteroids with controlled size and high reproducibility, particularly useful for cancer modelling and preclinical drug screening.[29]

Despite the promising anticancer effects of ATO and D-VC, one of the primary concerns can be a poor bioavailability, as both compounds have limited stability under physiological conditions. ATO, for instance, undergoes rapid clearance and may not reach therapeutic concentrations in solid tumours. ATO has well-documented dose-dependent toxic effects, including cardiotoxicity,[32] hepatotoxicity,[33] and neurotoxicity,[34] which restrict its use in high doses. D-VC is less potent in inducing oxidative stress than its natural form, VC, potentially reducing its efficacy. To overcome these limitations, targeted drug delivery systems are being explored[35,36] which are even more essential in the context of solid tumour treatment.[37] Smart nanoparticle drug delivery systems significantly improve the therapeutic potential of drugs by enhancing permeability and controlled release.[45] Encapsulation strategies, such as using enzyme-coated shellac nanoparticles, represent a significant advancement in targeted drug delivery, addressing challenges like drug instability, poor bioavailability, systemic toxicity and improving tumour-specific accumulation.[38]

Shellac, an FDA-approved natural resin, offers biocompatibility and pH-responsive properties due to its hydroxyl and carboxyl groups. Recent examples include chitosan-coated zein/shellac nanoparticles for quercetin delivery, demonstrating high encapsulation efficiency and controlled release kinetics.[39,40]

Curcumin-loaded shellac nanoparticles of high encapsulation efficiency and enhanced bio accessibility and stability across pH, temperature, and storage conditions have also been reported.[41,54] Enzyme functionalized shellac based nanocarriers of antibiotics have already been used to clear bacterial and fungal biofilms by digestion of the biofilm matrix.[55–59] Recently, Paunov *et al.* developed lysozyme-coated metformin-loaded nanoparticles of high drug encapsulation efficiency (over 90%) and enhanced anticancer effects in both 2D and 3D hepatic cancer cell cultures.[38,42,43]

In this study, we surface functionalised ATO/D-VC loaded shellac nanoparticles with the cationic protease Savinase 16L. This enzyme coating promotes active tumour targeting through electrostatic adhesion to the negatively charged cancer cells and facilitates better penetration in a 3D cell culture, loosening up the ECM, leading to enhanced therapeutic outcomes. By ensuring sustained and localized drug release, these nanocarriers can maximize therapeutic efficacy while minimizing adverse effects, making them an attractive solution for improving ATO and D-VC-based cancer therapies (see Scheme 1). ATO and D-VC-loaded Savinase-coated shellac nanoparticles were evaluated for their physicochemical properties such as particle size, surface charge, morphology, encapsulation efficiency, and release kinetics under physiological and tumour-mimicking conditions. Testing the delivery of ATO/D-VC using protease-functionalized nanocarriers was performed on 2D and optimized 3D cultures of CRC cell lines to compare the cytotoxic effects of the combination of ATO and D-VC in free and encapsulated forms.

Materials and methods

Materials

Deionised water (DI) purified by reverse osmosis and ion exchange from a Barnstead Smart2Pure water purification system (ThermoFisher Scientific, KZ) was used in all our studies. Its surface tension was 71.9 mN m^{-1} at 25 °C, with measured resistivity less than 18 MΩ cm^{-1}. Shellac was used in a soluble form as the ammonium salt (SSB AquaGold™, 25 wt% solid) at pH > 7. The ammonium shellac solution was a gift from Harke Pharma GmbH (Germany). Reagents for cell culture: Dulbecco's modified Eagle's medium (DMEM, Gibco, cat. no. 11965092); DMEM/F-12 (Gibco cat. no. 11320033); Fetal Bovine Serum (FBS) (Gibco cat. no. A5256701); penicillin–streptomycin (VWR Chemicals cat. no. 392-0406); Dulbecco's phosphate-buffered saline (PBS) (10×) (Capricorn Scientific PBS-10XA); Trypsin-EDTA (0.05%) (Capricorn Scientific cat. no. TRY-1B); and Cellstripper (Corning cat. no. 25056CI).

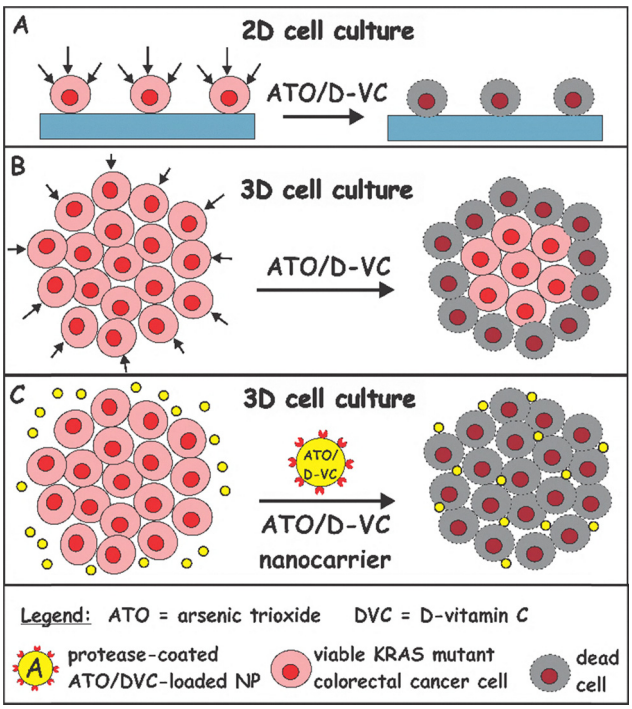

Scheme 1 Principle of action of the Savinase-coated ATO/D-VC nanocarrier on 3D cell clusters and solid tumours for enhanced drug delivery. Both ATO and D-VC independently elevate ROS levels and D-VC plays a significant chemosensitizing role; their combined use generates an amplified oxidative burst that exceeds the antioxidant capacity of cancer cells, leading to suicidal ROS production by mitochondria followed by irreversible damage and apoptosis. However, the ATO/D-VC combination exhibits reduced efficacy in 3D CRC culture models (B) compared to its action on 2D cultures (A) due to limited drug penetration through the ECM. It is anticipated that ATO/D-VC will affect mainly the peripheral cells in 3D clusteroids, with reduced impact on the core cells. Therefore, here we developed and tested Savinase-coated shellac nanoparticles with encapsulated ATO and D-VC for targeted CRC therapy (C).

Reagents for preparing cell clusteroids: poly(ethylene oxide) average M_v 200 000 (Sigma-Aldrich cat. no. 181994) and dextran M_W 250 000 (ThermoFisher cat. no. J60200.36). Reagents used for treatment: D-(−)-isoascorbic acid (D-VC, Sigma-Aldrich cat. no. #856061) and arsenic trioxide (ATO, Sigma-Aldrich cat. no. #A1010). Reagents for nanoparticle formulation: protease from *Bacillus* sp. (Sigma-Aldrich cat. no. P5985-50ML) and Poloxamer 407 (Sigma-Aldrich cat. no. 16758). Reagents for viability and cell proliferation evaluation: CellTiter 96® AQueous One Solution Reagent (Promega cat. no. G3580); Hoechst 33342 (ThermoFisher cat. no. H1399); propidium iodide (PI, ThermoFisher, cat. no. P1304MP); and DMEM/F-12, no Phenol Red (Gibco cat. no. 21041025). Reagents for flow cytometry: Annexin Binding Buffer 1× (ABB, ThermoFisher, cat. no. V13246), Annexin V-Alexa 647 (ThermoFisher, cat. no. A23204), propidium iodide (PI, ThermoFisher, cat. no. P3566), MitoSOX™ Red mitochondrial superoxide indicator (ThermoFisher, cat. no. M36008), MitoTracker™ Green FM (ThermoFisher, cat. no. M7514), and MitoTracker™ Deep Red FM (ThermoFisher, cat. no. M22426). Other chemicals used: L-ascorbic acid (Sigma-Aldrich, ≥99%, CAS no. 50-81-7) and sodium molybdate solution (Sigma-Aldrich, CAS no. 7631-95-0). Rhodamine 6G was sourced from Sigma-Aldrich, KZ.

Methods

2D cell culture

Human colorectal cancer cell lines were used in this research: HCT116, derived from human colorectal carcinoma, and SW620, derived from a lymph node metastasis of colorectal adenocarcinoma. Cell lines were sourced from ATTC (USA) and were cultured in DMEM supplemented with 10% FBS and 1% penicillin–streptomycin (10 000 U mL^{-1}) solution at 37 °C and 5% CO_2 in a humidified incubator. For 2D cell cultures, HCT116 or SW620 were seeded in tissue culture-treated 6-well plates at initial densities of 200 000 and 600 000 cells per well, respectively, and left for 48 h before treatment.

3D cell culture

To generate 3D clusteroids from the HCT116 or SW620 cell lines, a modified version of the water-in-water ATPS based emulsion protocol was used.[30,38,42,43,46] Briefly, a 30 wt% solution of 200 kDa poly(ethylene oxide) (PEO) in Dulbecco's PBS was prepared and sterilized through autoclaving. The sterile 30 wt% PEO solution was then diluted to 15 wt% and 7.5 wt% using DMEM supplemented with 20% FBS. After the dilutions, the resulted PEO solutions were then centrifuged at 7800 rpm for 3 h to remove the residual silica particles added by the manufacturer. A 450 kDa dextran (DEX) solution was prepared at a concentration of 7.5 wt% in DMEM with 10% FBS and sterilized by passing it through a 0.22 μm pore size syringe filter. Trypsinised HCT116 or SW620 cells were transferred to 1.5 mL Eppendorf tubes (200 000 and 800 000 cells per tube, respectively, to match 2D seeding densities) and centrifuged, and the resulting pellets were re-suspended in 20 μL of the 7.5 wt% DEX solution. Next, 80 μL of the 7.5 wt% PEO solution was layered over the DEX phase. A single-channel pipette (20–200 μL) was used to mix the solutions and form a DEX-in-PEO Pickering emulsion by pumping the mixture twice. An additional 900 μL of 15 wt% PEO was then added to the bottom of the tubes, and the clusteroids were left to settle naturally for 24 h in the incubator. After sedimentation, the tubes were centrifuged, and 200 μL of the clusteroid pellets was transferred into each well of ultra-low attachment 24-well plates. To break the DEX-in-PEO emulsion, 2 mL of DMEM supplemented with 10% FBS was added. 24 h after transferring the clusteroids from the tubes to the plates, the DMEM was refreshed, and the clusteroids were treated.

ATO and D-VC preparations

ATO and D-VC stock solutions were prepared as described previously.[2] A 340 mM stock solution of D-VC and 30 g of D-VC powder were dissolved in 400 mL of sterile phosphate-buffered saline (PBS). After complete dissolution, 39 g of sodium bicarbonate ($NaHCO_3$, catalogue #S5761) was added while stirring continuously for 5 min. Sodium bicarbonate

served as a buffering agent to neutralize the acidity of the solution (initial pH ≈ 2.3), adjusting it to a physiological pH of approximately 7.35. The final volume was brought up to 500 mL with additional PBS. The prepared D-VC stock solution was sterilized by filtration through a 0.22 μm syringe filter, aliquoted, and stored at −20 °C to preserve its stability and activity. For ATO, a 330 mM stock solution was prepared by dissolving 13 g of arsenic trioxide in 1 M sodium hydroxide (NaOH) with gentle stirring. The final volume was adjusted to 200 mL. This solution was also sterile-filtered and stored at −20 °C until use. The cells in both 2D and 3D cultures were treated with 7.5 μM ATO and 1.5 mM D-VC by replacing the existing culture medium with fresh DMEM/F12 supplemented with 10% FBS and drugs. The duration of treatment was 48 h.

Nanoparticle (NP) preparation, ATO and D-VC loading and coating with Savinase

Among the various nanoparticle systems, polymer-based carriers such as shellac nanoparticles stand out due to their inherent stability, biocompatibility, and capacity for controlled drug release. Shellac nanoparticles are commonly synthesized through pH-induced co-precipitation. At an alkaline pH of approximately 10, shellac remains soluble and is combined with the water-soluble drug. When the pH is subsequently reduced to around 4–5.5, shellac precipitates, entrapping the drug within the forming nanoparticle matrix. This approach yields a high drug-loading efficiency, often exceeding 90%.[38] To enhance colloidal stability and minimize nanoparticle aggregation, Poloxamer 407—a triblock copolymer surfactant—was employed as a stabilizing agent. In addition to improving dispersion, Poloxamer 407 enhances biocompatibility and may contribute to prolonged systemic circulation *in vivo*.[38,46] To formulate the nanoparticle system, we adapted the protocol developed by Wang *et al.*[38] for metformin encapsulation into lysozyme-coated shellac–poloxamer 407 nanocarriers. This protocol was modified to encapsulate ATO and D-VC within shellac–poloxamer 407 nanoparticles coated with Savinase (serine protease) to enhance their stability and effectiveness.

Unloaded NPs: shellac–poloxamer nanoparticles were formulated using a pH-driven precipitation method.[38,54] For uncoated and unloaded nanoparticles, a 0.6 wt% shellac solution was prepared by diluting the commercial 25 wt% shellac stock solution with DI water under constant stirring until fully dissolved. The solution was stored at 4 °C and used within 48 h. Poloxamer 407 powder was dissolved in DI water to a final concentration of 0.3 wt%. The solution was stirred until fully dissolved and stored at 4 °C. To prepare unloaded nanoparticles, 0.3 wt% poloxamer 407 and 0.6 wt% shellac were mixed in a 1 : 1 ratio, and DI water was added to yield final concentrations: 0.067 wt% Poloxamer 407 and 0.133 wt% shellac. The pH was increased to 10 using 0.25 M NaOH to solubilize the Poloxamer and the mixture was sonicated using a Branson SFX550 probe sonicator at 35% amplitude (15 s on, 15 s off) for a total of 1 min 15 s. The pH was then lowered to 2.5–2.75 with 0.25 M HCl. If visible aggregates formed, the suspension was sonicated again at 20% amplitude for 1 min to ensure proper dispersion. Finally, the pH was increased to 5 to avoid aggregation. The formulation was sterilized by filtration through a 0.22 μm syringe filter. ATO-loaded NPs: for ATO-loaded NPs, 1 mL of 0.3 wt% poloxamer, 1 mL of 0.6 wt% shellac, and 2.054 mL of DI water were mixed. After pH elevation to 8 and sonication, 446 μL of 5.05 mM ATO solution was added. The pH was then decreased to 2.5–2.75 and finally adjusted to 5 before filtration. D-VC-loaded NPs: to prepare D-VC-loaded NPs, 1 mL of 0.3 wt% poloxamer 407, 1 mL of 0.6 wt% shellac, and 1.885 mL of DI water were used. After 5 min of sonication in a sonic bath and pH adjustment above 7.0, 615 μL of 330 mM D-VC solution was added. The pH was first lowered to 2.5–2.75 and then adjusted to 5. The formulation was filtered as described above. Savinase coating of NPs: a 0.6 wt% Savinase stock solution was prepared by diluting 0.6 mL of liquid Savinase® 16L stock from the manufacture with DI water to a final volume of 100 mL. The solution was sonicated in an ultrasonic bath for 15 min to minimize enzyme aggregation before use. For coating of unloaded, ATO-loaded, and D-VC-loaded NPs, 1 mL of NP suspension was centrifuged at 14 500 rpm for 15 minutes, the supernatants were discarded, and the pellets were resuspended in 1 mL of 0.6 wt% Savinase solution at pH 5. After 30 min of gentle shaking, the samples were centrifuged again at 15 000 rpm for 15 min to remove unbound components and collect the Sav-functionalized nanoparticles and resuspended in 1 mL of DMEM/F12 medium supplemented with 10% FBS for downstream use.

Characterization of Sav-coated ATO and D-VC loaded shellac NPs

The hydrodynamic diameter and zeta potential were measured *via* dynamic light scattering (DLS) using a Litesizer 500 (Anton Paar GmbH, Austria). The optimal concentration was selected based on achieving a positive surface charge without evidence of aggregation. The zeta potential of both uncoated nanoparticles and free Savinase was measured at pH 3 to 7 at 25 °C. To confirm successful coating the prepared Savinase-coated nanoparticle size was measured by DLS, and the nanoparticles were visualized by scanning electron microscopy (SEM). Additionally, to assess their interaction with 3D cell structures, HCT116 clusteroids were incubated with unloaded Savinase-coated nanoparticles for 4 hours, fixed, and imaged using SEM to observe nanoparticle accumulation on the cell surface. To assess the morphology of cells in 2D and 3D cultures, their growth and drug-induced morphological changes, brightfield microscopy images were acquired using an Olympus CKX53 fluorescence microscope. The size of individual clusteroids was measured using ImageJ by manually tracing and analyzing each clusteroid from the acquired images. Fluorescence microscopy was used to assess the cell viability (see appropriate section of M&M). A confocal laser scanning microscope (CLSM, Zeiss LSM780) was used to assess the ability of Savinase as a protease coating to enhance nanoparticle penetration through the ECM, thereby improving drug delivery to tumor cells. Sav-coated NPs were loaded with

Rhodamine B (100 μM) and cell nuclei were pre-stained with 1 mg mL^{-1} Hoechst 33342.

Scanning electron microscopy was also used to image clusteroids covered with NPs. Clusteroids were extracted from the emulsion by adding PBS, which disrupted the emulsion droplets. The resulting mixture was centrifuged, and the collected clusteroids pellet was washed twice with PBS to eliminate residual polyethylene glycol (PEG), dextran, and culture medium. The washed clusteroids were then fixed in a 1% (w/v) glutaraldehyde solution for 2 hours at room temperature, followed by washing with DI water. Following fixation, the samples were air-dried overnight and subsequently imaged using a scanning electron microscope ZEISS Crossbeam 540 (Germany) after coating with a gold/platinum layer.

ATO quantification

To perform quantitative analysis of arsenic trioxide, As_2O_3 (ATO), in release studies, a calibration curve was determined using serial dilutions of a 5050 μM ATO stock solution. Standard solutions were prepared with DI water to yield final concentrations of 0, 5, 10, 15, 20, 30, 40, and 50 μM. For colorimetric detection, 500 μL of each standard solution was transferred to 1.5 mL Eppendorf tubes. Each sample was sequentially mixed with 40 μL of 5 N sulfuric acid (H_2SO_4) and 40 μL of 10% (w/v) L-ascorbic acid (Sigma-Aldrich KZ, ≥99%, CAS no. 50-81-7) and incubated at room temperature for 30 min to facilitate complete reduction of As^{5+} to As^{3+}. Subsequently, 40 μL of 20% (w/v) sodium molybdate solution was added to initiate formation of the arsenomolybdate complex. Each reaction mixture was dispensed in triplicate (100 μL per well) into a flat-bottom 96-well microplate. The plate was incubated for an additional 30 min at room temperature to allow full colour development prior to measurement. Absorbance was then recorded at 880 nm using a FLUOstar Omega microplate reader (BMG Labtech, UK). DI water and 0 μM ATO samples were used as blanks. A standard curve was generated by plotting absorbance against ATO concentration, and a linear regression equation was derived to calculate unknown ATO concentrations in release assays.

Release kinetics of ATO from ATO-loaded shellac nanoparticles

Uncoated ATO-loaded shellac–poloxamer NPs were prepared as previously described. A total of 20 mL of NP suspension was centrifuged at 14 500 rpm for 15 min, and the pellet was resuspended in 20 mL of DI water. The suspension was transferred into a pre-hydrated cellulose membrane for dialysis (12–14 kDa pore size), which was then submerged in 50 mL of DI water in a glass beaker. The release system was maintained at room temperature under gentle stirring throughout the experiment. At predetermined time points (0, 1, 2, 3, 4, 5, 6, 12, 24, 36, and 48 h), 1 mL of dialysate was withdrawn and immediately replaced with an equal volume of fresh DI water to maintain sink conditions. Prior to measurement, samples were diluted 1:4 with DI water, and the ATO concentration was determined using the same colorimetric method described above. Absorbance values were converted to concentration using the calibration equation, and cumulative release profiles were plotted as a function of time.

Determination of ATO encapsulation efficiency in shellac NPs

The encapsulation efficiency of ATO in shellac–poloxamer NPs was assessed by quantifying the unencapsulated ATO remaining in the supernatant after NPs formulation. As described previously, ATO-loaded, uncoated NPs were prepared and centrifuged at 14 500 rpm for 15 min to pelletize the NPs. The supernatant, containing free ATO, was collected and diluted 1:4 with DI water. Quantification of ATO in the supernatant was performed using the previously described colorimetric assay. ATO concentrations were determined using the established calibration curve. The initial ATO concentration used for NP formulation was $[ATO]_{total}$ = 500.5 μM, calculated based on the total amount of ATO added during synthesis. The encapsulation efficiency (E.E.) was determined using the following equation:

$$\text{E.E. } (\%) = \left(\frac{[ATO]_{total} - [ATO]_{free}}{[ATO]_{total}}\right) \times 100,$$

where $[ATO]_{free}$ represents the concentration of unencapsulated ATO in the supernatant. The encapsulation efficiency was evaluated in three independent nanoparticle preparations to assess consistency and reproducibility.

D-VC quantification

A stock solution of D-VC was serially diluted with DI water to prepare concentrations of 0.5, 1, 2, 4, 6, 8, 10, 12, and 15 mM. A 5 mM DCPIP (2,6-dichlorophenolindophenol sodium salt) solution was freshly prepared each time by dissolving 14.5 mg of DCPIP sodium salt (M_W = 290.1 g mol^{-1}) in 10 mL of DI water. Either 20 or 25 μL of each D-VC dilution was dispensed into designated wells of a 96-well plate in triplicate. For the 0 mM D-VC control, the same volume of DI water was added instead of D-VC. DI water (80 or 75 μL, respectively) was added to each well to adjust the total pre-DCPIP volume to 100 μL. Subsequently, 100 μL of 5 mM DCPIP was added to each well. Absorbance was recorded immediately after DCPIP addition at 520 nm. Wells containing 200 μL of Milli-Q water served as the blank control. Absorbance was plotted *versus* the D-VC concentration up to 10 mM, where the graph is linear and used as a calibration graph for quantification of free D-VC in the solutions and supernatants in our experiments. The evaluation of the release kinetics of D-VC from the nanocarriers is described in the SI.

D-VC encapsulation efficiency and release kinetics from Sav-NPs

D-VC dialysis was performed exactly like ATO dialysis, with only the difference that each aliquot was covered with parafilm and stored in a −20 °C freezer to prevent further oxidation. Prior to the DCPIP assay, the samples were diluted 1:4 with DI water (the same as with ATO). Aliquots for the E.E. test were taken before NPs were prepared for the D-VC release kinetics by using a dialysis-based setup. Both E.E. and the release tests by dialysis were carried out as independent triplicates (ran

simultaneously). The sampling and the absorbance measurements were also carried out in technical triplicates. During the 48 hours of the experiment, the beakers were flushed with a stream of N_2 every 3–6 hours and kept sealed with parafilm in between samplings to avoid oxidation of D-VC. To find the D-VC concentrations, a calibration curve equation was used (Fig. S1B, SI). The obtained D-VC concentrations in each sample, which fell into the range between 0 and 5.5 mM, were multiplied by the dilution factor of 4 to recover the real concentrations.

Proliferation and viability assays

Post treatment, both 2D and 3D cell cultures were collected. Cells in monolayers were harvested using trypsin/EDTA, while 3D clusteroids were disassembled with a StemPro™ Accutase™ Cell Dissociation Reagent. The action of the trypsinizing reagents was neutralized with DMEM containing 10% FBS without Phenol Red. To measure the cell proliferation rate after treatment, we used the CellTiter 96 AQueous one solution cell proliferation assay (MTS). Equal volumes of treated and control cell suspensions were transferred into tissue culture-treated 96-well plates and stained using the MTS assay kit. Absorbance was measured after 1 h of incubation using the FLUOstar Omega Microplate Reader. The relative percentage of cell proliferation was calculated in comparison with the control. For cell viability assessment, the Hoechst/PI assay was used. Collected cells were transferred into tissue culture-treated 96-well plates and stained with 2 μM Propidium Iodide (PI) and 0.2 μM Hoechst 33342 for 40 minutes. Images were captured using an Olympus CKX53 inverted microscope equipped with a U-RFL-T power supply for the mercury burner. The number of dead cells and the total number of cells in the images were quantified using ImageJ software.

The percentage of cell viability was calculated as follows:

$$\%\text{Viable cells} = \left(1 - \frac{\text{Number of dead cells}}{\text{Number of total cells}}\right) \times 100\%$$

Flow cytometric analysis of apoptosis and mitochondrial function

For flow cytometric assays, cells were harvested as described above and counted using a Nexcelom X2 automated cell counter (Revvity, Bradford, UK). To assess induction of apoptosis, adherent and floating apoptotic cells were combined. The cell suspension was washed once with PBS, and the cell density was adjusted to 1×10^6 cells per mL with 1× Annexin Binding Buffer (ABB). A 100 μL aliquot of the 1×10^6 cells per mL suspension was stained with 3 μL of Annexin V-Alexa 647 and 1 μL of Propidium Iodide (PI) for 15 min at room temperature in the dark. Afterwards, 400 μL of ABB buffer was added, and samples were kept on ice until analysis. For mitochondrial function assays, 5×10^5 cells were stained with a MitoSOX™ Red mitochondrial superoxide indicator (2.5 μM), MitoTracker™ Green FM (150 nM), and MitoTracker™ Deep Red FM (50 nM) for 30 min at 37 °C. Samples were acquired using an Attune NxT Flow Cytometer (ThermoFisher, cat. no. A24858).

For the apoptosis assay, a minimum of 30 000 events were acquired, and for mitochondrial assays, a minimum of 10 000 events were recorded per sample.

Statistical analysis

All experiments were performed in a minimum of biological triplicates. Data are expressed as mean ± standard deviation (SD) unless otherwise indicated. Statistical analyses were performed using GraphPad Prism (version 10.5.0, GraphPad Software, USA) or equivalent statistical software. Differences in treatment responses between 2D and 3D cell cultures, as well as between free ATO/D-VC and ATO/D-VC encapsulated in nanoparticles, were assessed using one-way ANOVA followed by Tukey's *post hoc* test for multiple comparisons. A p-value less than 0.05 was considered statistically significant and was indicated directly in the corresponding figures using standard asterisk notation, $P < 0.05$ (*), $P < 0.01$ (**), $P < 0.001$ (***), and $P < 0.0001$ (****).

Results and discussion

Development and characterization of enzyme-coated nanoparticles for enhanced oxidative therapy in 3D cultures

To enhance the efficacy of oxidative drug treatment in 3D cultures, we designed a novel nanoparticle-based delivery system composed of protease-coated shellac nanocarriers loaded with ATO and D-VC (Fig. 1(A)). This approach was developed to overcome the limited drug penetration and reduced redox sensitivity observed in clusteroid models. Comprehensive physicochemical characterization was conducted to optimize pH conditions and enzyme concentration for effective surface functionalization. DLS analysis showed an increase in hydrodynamic diameter with enzyme coating, indicating surface deposition of the enzyme without significant aggregation (Fig. 1(B)). Zeta potential analysis of the Savinase-coated shellac NPs (Sav-coated NPs) across a pH range revealed that pH 5 provided the most favourable conditions for electrostatic binding because at this pH, Savinase exhibited a positive surface charge (zeta-potential +15 mV), while the uncoated nanoparticles retained a negative surface charge (zeta-potential −19 mV), promoting electrostatic interaction (Fig. 1(C)). Upon coating, the zeta potential of the shellac NPs gradually increased with increasing Savinase concentrations, plateauing above 0.5–0.6 wt%, indicating saturation of available binding sites on the particle's surface. A concentration of 0.6 wt% Savinase was selected for all further experiments. Imaging with SEM confirmed well-defined morphology of both ATO and D-VC loaded NPs, with an average dry particle diameter of 190–200 nm (Fig. 1(E) and (F)). This size was consistent but slightly lower than the one from DLS measurements (~270 nm), likely due to shrinkage upon drying during SEM sample preparation. To determine the encapsulation efficiency (E.E.%) of ATO within ATO-loaded shellac NPs, we employed an indirect quantification method. After the NPs synthesis and purification *via* centrifugation and washing to remove the

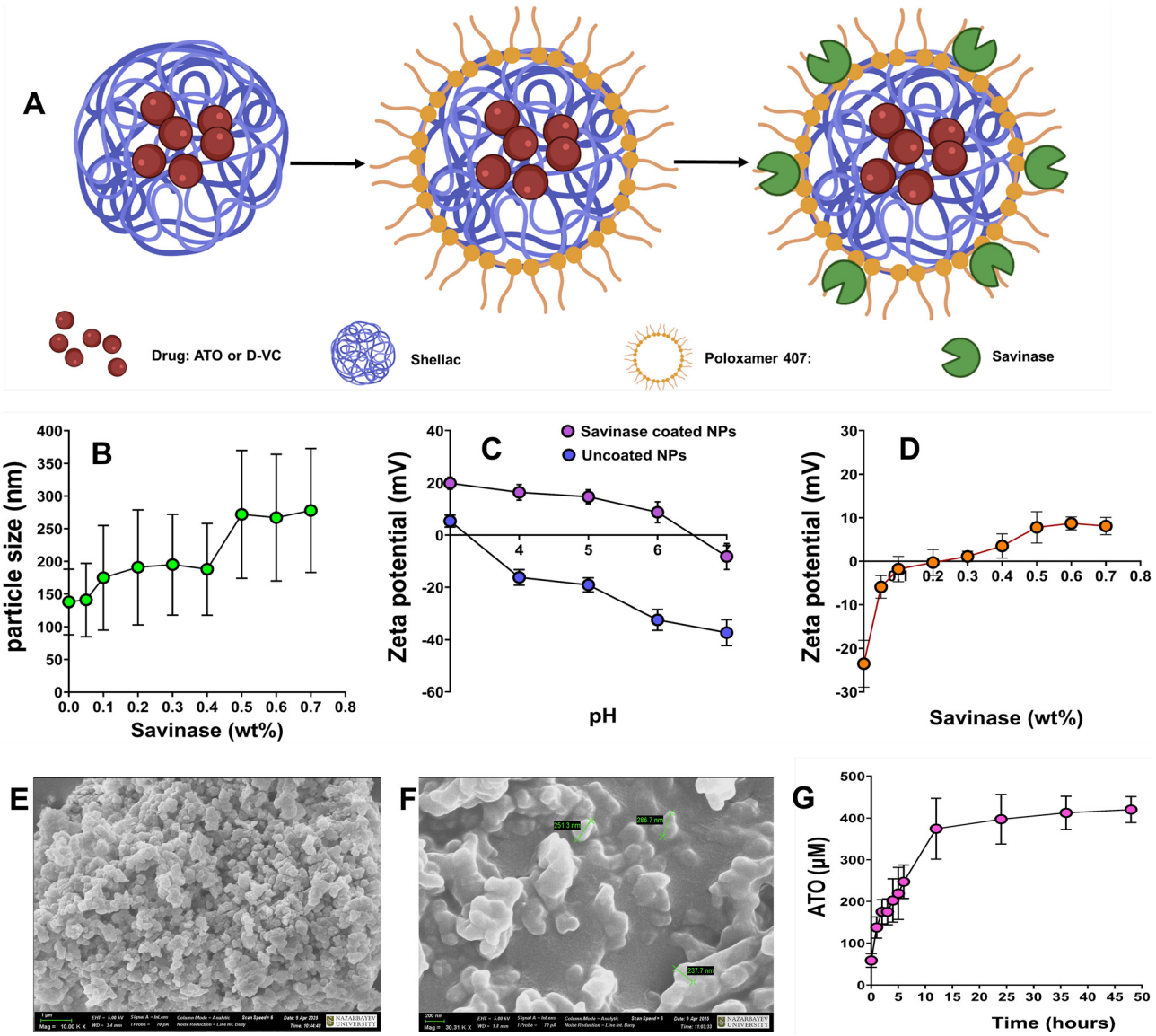

Fig. 1 (A) Schematics of nanoparticle formation and coating. (B) Mean particle hydrodynamic diameter measurements of the Sav-coated ATO loaded nanoparticles (NPs) as a function of the Savinase coating concentration at pH 5. Here, the vertical bars represent the particle size standard deviation. (C) The zeta potential of uncoated and Sav-coated shellac NPs as a function of pH, showing the uncoated and Sav-coated shellac particles' isoelectric point. Error bars represent the standard deviation of the mean value measurements (n = 3). (D) Mean zeta potential of the Sav-coated ATO loaded NPs *versus* the Savinase coating concentration at pH 5. Scanning electron microscopy (SEM) images of Sav-coated NPs loaded with ATO (E) and D-VC (F), highlighting particle morphology, surface texture, and size distribution after drug loading and enzyme coating. (G) Cumulative ATO release curve from ATO-loaded shellac NPs measured with the colorimetric molybdenum blue method using dialysis.

unencapsulated drug, the concentration of free ATO in the supernatant was measured using the molybdenum blue colorimetric assay for arsenic detection. The ATO loaded NPs demonstrated high encapsulation efficiency, with an average E.E.% of 87.1% (ranging between 83% and 89%). This high efficiency reflects the strong interaction between ATO and the NP matrix and indicates the suitability of the shellac NP system for effective intracellular delivery of oxidative agents like ATO.

To evaluate the *in vitro* release profile of ATO from the shellac NPs and gain a better insight into the timescale of its release from the nanocarrier upon dilution, we performed an *in vitro* release study under physiologically relevant conditions. The concentration of released ATO in the supernatant was quantified using the molybdenum blue method as previously outlined in Methods. Using the calibration graph in Fig. S1A (SI), the ATO concentration was estimated from the sample absorbance. The cumulative release profile (Fig. 1(G)) exhibited a biphasic pattern, characterised by a burst release of ~80% ATO within the first 12 h, followed by a gradual further release up to 48 h. This release behaviour ensures prolonged intracellular availability of ATO, improving its therapeutic potential while minimising systemic toxicity. The D-VC encapsulation efficiency in Sav-NPs was found to be 75.8 ± 0.8%. The release curve of D-VC from Sav-coated D-VC loaded shellac NPs is

presented in Fig. S1C (SI). One can see that over 90% of the loaded D-VC is released in the first 10 hours of the experiment. This finding is similar to the ATO release (Fig. 1(G)), where it takes 12 h to release 80% of the encapsulated drug.

Formation and growth assessment of 3D clusteroids

The 3D clusteroids were generated out of HCT116 and SW620 cells using DEX-in-PEO ATPS emulsification (Fig. 2(A)) following optimisation (Fig. S2, SI). The growth of clusteroids was monitored over a 6-day period. Representative brightfield images revealed a gradual and consistent increase in size and density for both HCT116 and SW620 clusteroids (Fig. 2(B)). Quantitative statistical analysis confirmed a significant increase in clusteroid size from day 2 to day 6 for both cell lines (Fig. 2(C)), supporting active proliferation and structural maturation. To standardize treatment response experiments, clusteroid sizes were measured after 48 h of culture (pre-treatment), and analysis demonstrated uniform size distribution across all experimental groups (Fig. 2(B) and Fig. S3, SI), ensuring comparability in subsequent drug testing.

Penetration of Sav-coated nanoparticles into the clusteroid core

To examine nanoparticle–cell interactions, SEM imaging was performed on HCT116 cells grown as 3D clusteroids. Untreated controls exhibited smooth or folded plasma membranes, devoid of spherical nanostructures (Fig. 3(A) and (B)). In contrast, cells treated with unloaded Sav-coated NPs displayed distinct roughening of the membrane and uniformly distributed particles ranging from 63–132 nm, consistent with the expected nanoparticle dimensions (Fig. 3(C) and (D)). SEM imaging of HCT116 clusteroids treated with Sav-coated NPs further demonstrated the presence of spherical particles adhering to the cell surface, hence the successful targeting. However, it should be noted that SEM imaging confirms the presence of the particles only on the peripheral cells of the clusteroids (Fig. 3(C) and (D)). To evaluate the ability of Sav-coated NPs to penetrate the inner regions of 3D tumour-like clusteroids, we employed confocal fluorescence microscopy using fluorescent tracer (Rhodamine 6G)-loaded Sav-NPs. After incubation, optical sectioning through the Z-stack of the clusteroids revealed significant fluorescence signal distributed not only at the periphery but also within the deeper layers of the 3D structures, indicating efficient NP penetration. The cationic nature of Savinase facilitates electrostatic interactions with the negatively charged components of tumour cell membranes or extracellular matrices. This interaction promotes a closer association with cancer cells, enhancing the uptake of NPs and improving the localized delivery of therapeutic agents.

A sustained Rhodamine B fluorescence signal was observed from the periphery toward the core of the clusteroid, suggesting

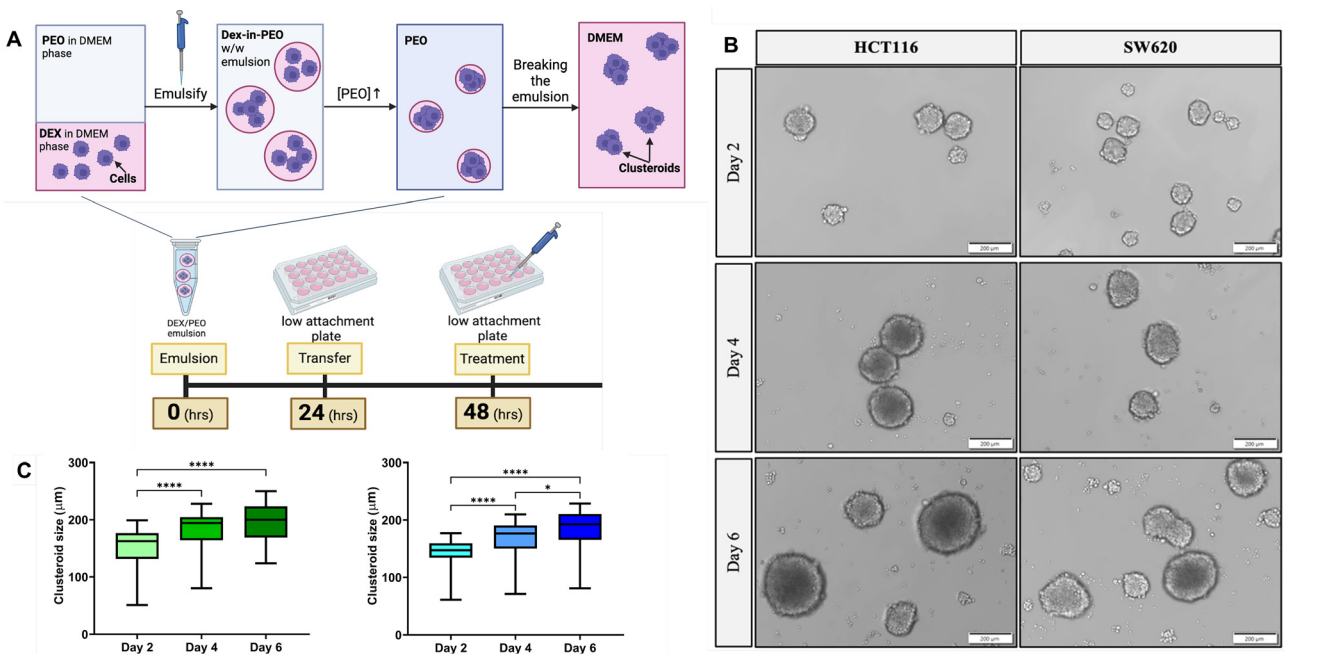

Fig. 2 Formation and growth of 3D clusteroids from HCT116 and SW620 colorectal cancer cell lines. (A) Schematic workflow illustrating the preparation of 3D colorectal cancer cell cultures. Clusteroids were generated using dextran/polyethylene oxide (DEX/PEO) aqueous two-phase emulsions and subsequently cultured in ultra-low attachment plates. Key time points are indicated: clusteroid formation (0 h), transfer to culture plates (24 h), treatment application (48 h), and sample collection (96 h). (B) Representative brightfield images showing the growth of 3D clusteroids derived from HCT116 (left panels) and SW620 (right panels) cell lines at days 2, 4, and 6 of cultivation. Both cell lines exhibit progressive increases in clusteroid size and compactness over time. Scale bars represent 200 µm. (C) Quantitative analysis of clusteroid size at different time points. Data are presented as mean ± standard deviation (SD) from three independent experiments, demonstrating the temporal growth dynamics of 3D clusteroids for both HCT116 and SW620 cell lines. Statistical significance was determined using one-way ANOVA with Tukey's *post hoc* test. Asterisks indicate statistically significant differences: $P < 0.05$ (*), $P < 0.01$ (**), $P < 0.001$ (***), and $P < 0.0001$ (****).

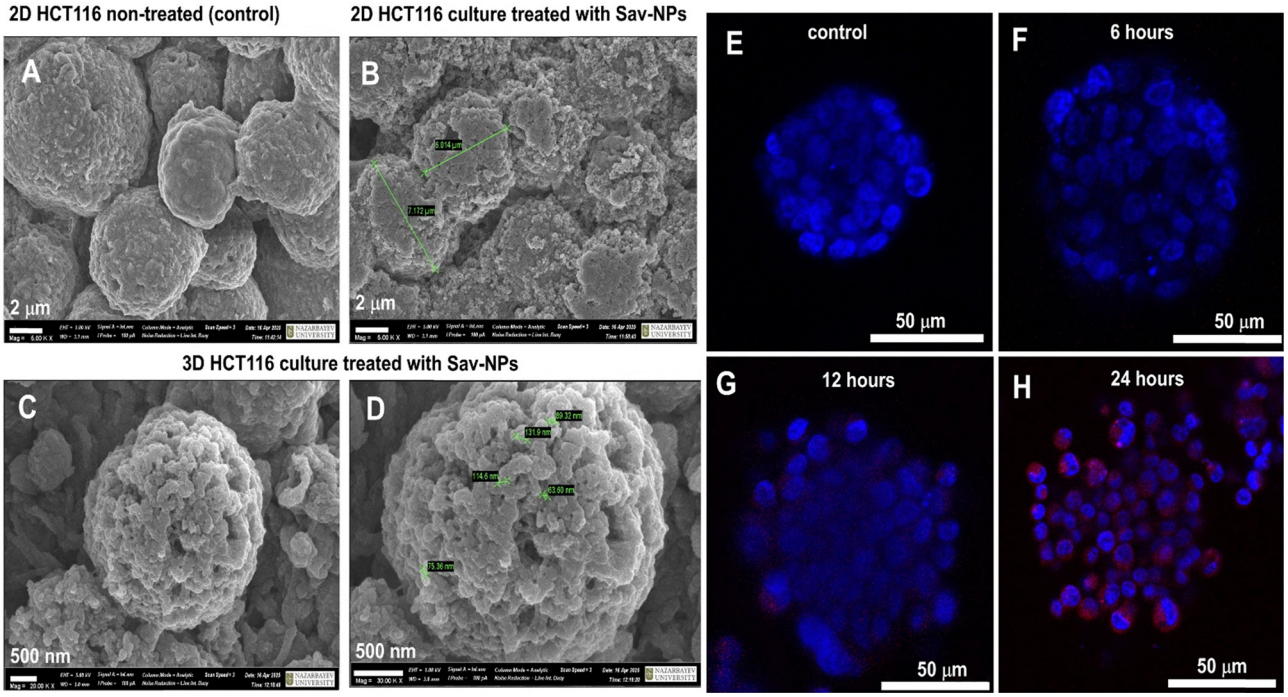

Fig. 3 SEM image comparison of untreated (A) and (B) and Savinase-coated NP-treated (C) and (D) 3D HCT116 colorectal cancer cells at different magnifications. In treated samples (C) and (D), numerous surface-bound nanoparticles are observed on the cell membrane, whereas the untreated controls lack such features, confirming successful cellular association of the Sav-coated NPs. (E)–(H) Penetration of Sav-coated NPs into 3D clusteroids *versus* time: CLSM images of Sav-coated NP penetration through ECM barriers to the 3D clusteroid core. Comparison of the control (E) with (F)–(H) Sav-coated NPs loaded with rhodamine B (as a fluorescent tracer) for visualisation of the NP penetration. Images indicate the red fluorescence after 6 h (F), 12 h (G) and 24 h (H). The cell nuclei are stained with Hoechst 33342 for cell co-localization purposes.

that Sav-coating facilitates deep tissue diffusion of the NPs. Compared to the untreated control (Fig. 3(E)), Sav-coated NPs exhibited markedly improved penetration to the clusteroid core, evidenced by the gradual accumulation of a red fluorescence signal on the cell surface of even the core cells, accompanied by loosening of the clusteroid structure (Fig. 3(F)–(H)). These findings suggest that Savinase surface functionalization enhances the NPs payload delivery into compact tumour cell clusteroid structures, overcoming one of the key limitations of nanotherapeutic delivery in solid tumour models.

Evaluation of free ATO and D-VC treatment combination in 2D and 3D CRC cultures

To investigate the cytotoxic effects of the oxidative drug combination ATO and D-VC in 2D monolayer cultures and 3D clusteroids of HCT116 and SW620 CRC cell lines, cells were treated with free ATO (7.5 μM), D-VC (1.5 mM), or their combination for 48 hours. Representative brightfield images are shown in Fig. 2(A) and 3(A) for HCT116 and SW620, respectively.

The combination of ATO and D-VC treatment in the 2D culture inflicted visible morphological changes, including reduced confluency, cell rounding, detachment, and shrinkage; however, such changes were not observed in each individual treatment arm or untreated control. Following similar treatment of 3D clusteroids with ATO (7.5 μM), D-VC (1.5 mM), or their combination, brightfield microscopy revealed that clusteroids maintained their compact and spherical morphology under ATO and D-VC single-drug treatments, with little or non-detectable morphological changes from the untreated controls. However, under combined ATO and D-VC treatment, slight peripheral cell disintegration and mild loosening of the clusteroid structure were observed, showing very little structural compromise (Fig. 4(A) and 5(A)).

Evaluation of Savinase-coated nanoparticles in 3D clusteroids

To assess the efficacy of nanoparticle-mediated delivery of oxidative drugs, HCT116 and SW620 clusteroids were treated with ATO and D-VC (7.5 μM/1.5 mM) delivered in different combinations, including free drugs, Savinase-coated unloaded NPs, and several Savinase-coated nanoparticle (Sav-NP) combinations.

The tested combinations included Sav-ATO NPs (Savinase-coated nanoparticles loaded with ATO), Sav-D-VC NPs (Savinase-coated nanoparticles loaded with D-VC), Sav-ATO NPs + D-VC (ATO-loaded Savinase-coated nanoparticles co-administered with free D-VC), and Sav-ATO NPs & Sav-D-VC NPs (a combination of two types of Savinase-coated nanoparticles, each separately loaded with ATO or D-VC, delivered together). Proliferation analysis using MTS assays showed that the ATO and D-VC combination significantly reduced cell proliferation, down to approximately 60% in HCT116 and below 40% in SW620 compared to untreated controls, corresponding to 1.7-fold and 2.5-fold reductions, respectively. In both cell lines, the combination's therapeutic effect was at least twice as potent as either drug alone. In 3D cultures, single-drug

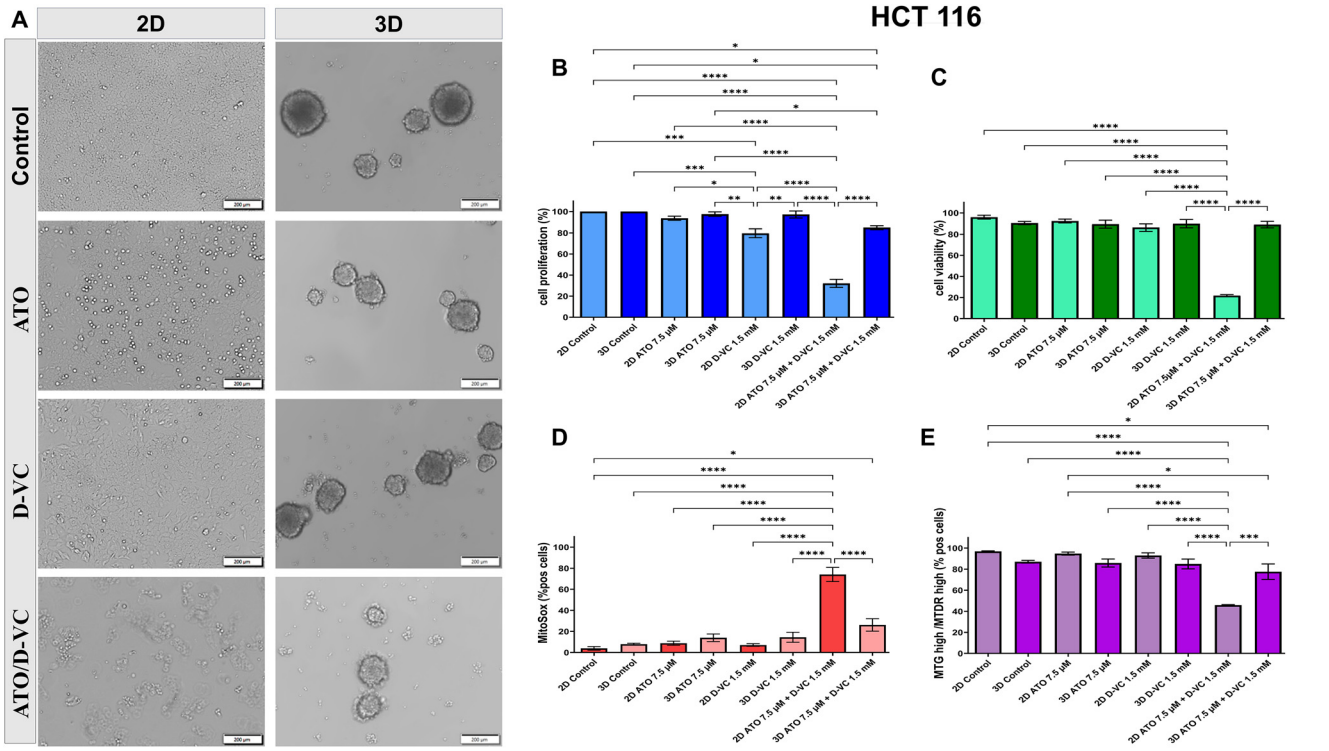

Fig. 4 Effect of oxidative drug combinations on HCT116 cells in 2D and 3D cultures. (A) Representative brightfield images of HCT116 colorectal cancer cells cultured under 2D monolayer and 3D clusteroid conditions following 48-hour treatment with four different regimens: untreated control, ATO (7.5 μM), D-VC (1.5 mM), and the combination of ATO and D-VC (7.5 μM/1.5 mM). Morphological changes are evident in the 2D culture in response to drug treatments, particularly with the combination therapy but not in the 3D culture. Scale bars: 200 μm. (B) Quantitative analysis of cell proliferation in 2D and 3D cultures after 48-hour treatment, as measured by MTS assay. Results are expressed as relative proliferation compared to untreated controls (%), highlighting the inhibitory effects of ATO, D-VC, and especially the combination treatment on cell growth in the 2D culture. (C) Assessment of cell viability following treatment, determined by dual Hoechst/PI staining. Data are presented as the percentage of viable (Hoechst-positive, PI-negative) cells, showing a significant reduction in viability in drug-treated groups in the 2D culture, with the most pronounced effect observed for the ATO/D-VC combination, but with minimal effectiveness in the 3D culture. (D) Measurement of mitochondrial ROS production using flow cytometry and MitoSOX Red staining. The percentage of MitoSOX-positive cells is shown for each treatment group, demonstrating increased ROS generation upon exposure to ATO and D-VC, with the combination treatment inducing the highest ROS levels, mainly in the 2D culture. (E) Analysis of mitochondrial function in treated cells, assessed by the proportion of cells double positive for MitoTracker Green (MTG, total mitochondria) and MitoTracker Deep Red (MTDR, polarised mitochondria). The percentage of MTG+/MTDR+ cells reflects the maintenance of functional mitochondria under each condition, with a marked decrease observed following combination treatment in the 2D culture, indicating mitochondrial dysfunction. All quantitative data are presented as mean ± standard deviation (SD) from a minimum of three independent biological replicates.

treatments had a limited effect and only a moderate effect of the ATO/D-VC free drugs combination on the proliferation was observed. Metabolic activity was reduced from 100% to ~85% in HCT116 and ~60% in SW620, representing 1.18-fold and 1.7-fold decreases, respectively (Fig. 4(B) and 5(B)). Cell viability assays further highlighted the increased free drug resistance of 3D cultures. In the 2D culture, the ATO and D-VC combination reduced viability to <30% in HCT116 and <25% in SW620, over three-fold reductions *versus* controls. In contrast, viability in HCT116 clusteroids declined by only ~10% and in SW620 by ~14% (Fig. 4(C) and 5(C)). Interestingly, SW620 cells displayed stronger responsiveness in both models, especially under combination treatment, while HCT116 appeared more resistant, particularly in the 3D structures.

Clusteroid size distribution before and after treatment is shown in Fig. S4 for HCT116 and Fig. S5 for SW620. To examine the underlying mechanism, we assessed mitochondrial dysfunction and ROS generation using flow cytometry with MitoSOX (for mitochondrial superoxide) and MitoTracker Green/Deep Red (for mitochondrial mass and membrane potential).

In 2D cultures, ATO and D-VC co-treatment led to a significant increase in the percentage of MitoSox positive cells, indicating robust ROS production and a significant decrease in the percentage of healthy mitochondria (MTG high/MTDR high). Together, across both cell lines HCT116 and SW620, the ATO and D-VC combination displayed enhanced efficacy in 2D cultures, where both proliferation and viability were suppressed to a greater extent than in the 3D culture.

Representative brightfield images (Fig. 6 and 7) illustrate the morphological impact of each treatment condition on the tested cell lines. In the untreated control and Savinase-coated unloaded NPs groups, clusteroids retained their spherical

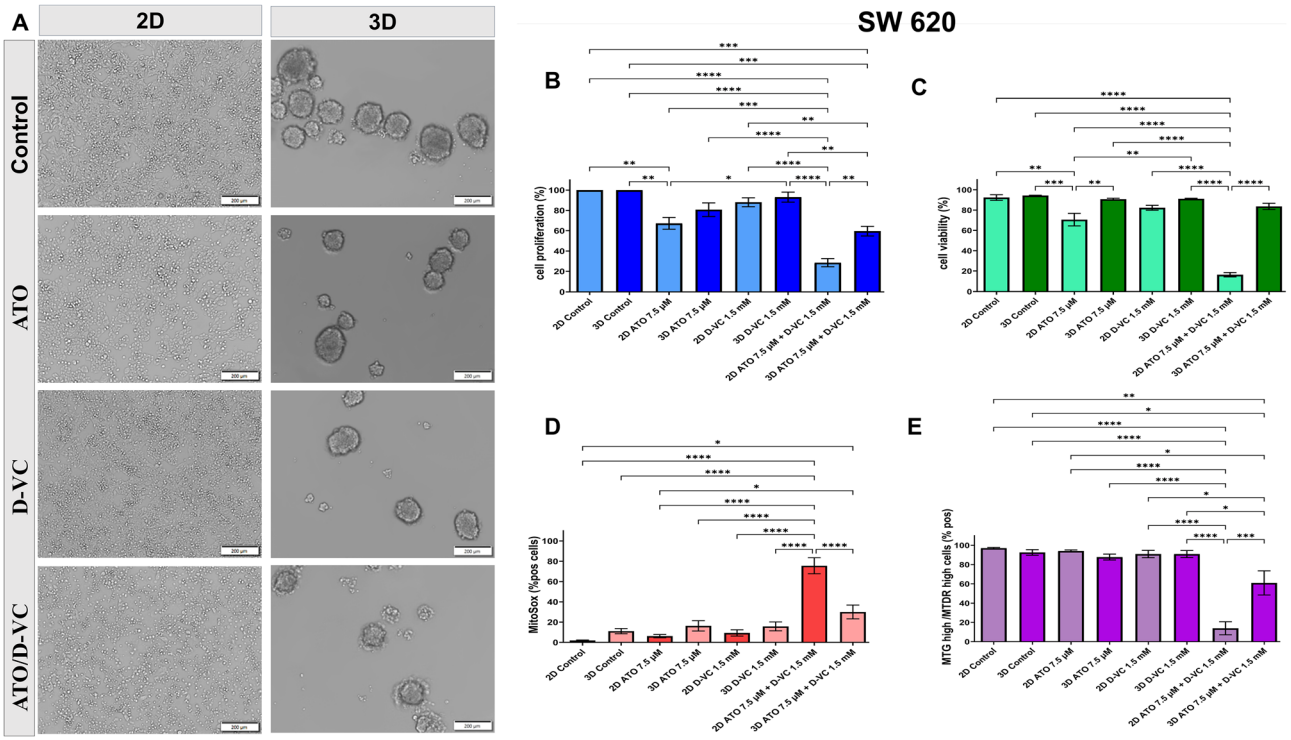

Fig. 5 Effect of oxidative drug combinations on SW620 cells in 2D and 3D cultures. (A) Representative brightfield images of SW620 colorectal cancer cells cultured under 2D monolayer and 3D clusteroid conditions following a 48-h treatment with four different regimens: untreated control, ATO (7.5 μM), D-VC (1.5 mM), and the combination of ATO and D-VC (7.5 μM/1.5 mM). Morphological changes are evident in the 2D culture in response to drug treatments, particularly with the combination therapy, but not in the 3D culture. Scale bars: 200 μm. (B) Quantitative analysis of cell proliferation in 2D and 3D cultures after 48-h treatment, as measured by MTS assay. Results are expressed as relative proliferation compared to untreated controls (%), highlighting the inhibitory effects of ATO, D-VC, and especially the combination treatment on cell growth in the 2D culture. (C) Assessment of cell viability following treatment, determined by dual Hoechst/PI staining. Data are presented as the percentage of viable (Hoechst-positive, PI-negative) cells, showing a significant reduction in viability in drug-treated groups in the 2D culture, with the most pronounced effect observed for the ATO/D-VC combination, but with minimal effectiveness in the 3D culture. (D) Measurement of mitochondrial ROS production using flow cytometry and MitoSOX Red staining. The percentage of MitoSOX-positive cells is shown for each treatment group, demonstrating increased ROS generation upon exposure to ATO and D-VC, with the combination treatment inducing the highest ROS levels, mainly in the 2D culture. (E) Analysis of the mitochondrial function in treated cells, assessed by the proportion of cells double positive for MitoTracker Green (MTG, total mitochondria) and MitoTracker Deep Red (MTDR, polarised mitochondria). The percentage of MTG+/MTDR+ cells reflects the maintenance of functional mitochondria under each condition, with a marked decrease observed following combination treatment in the 2D culture, indicating mitochondrial dysfunction. All quantitative data are presented as mean ± standard deviation (SD) from at least three independent biological replicates.

morphology with minimal disruption. Treatment with either Sav-ATO or Sav-D-VC NPs caused partial loosening and decreased compactness of the clusteroids. These effects were more pronounced when both agents were delivered together, either as a mixed formulation (Sav-ATO NPs with free D-VC) or as dual-loaded nanoparticles (Sav-ATO & Sav-D-VC NPs).

In HCT116 cells, proliferation inhibition in the 2D culture was over twice that seen in the 3D culture, and in SW620 cells, the difference approached two-fold as well ($p < 0.001$ and $p < 0.01$, respectively). A similar trend was observed for cell viability, with 2D cultures showing nearly two-fold greater reductions ($p < 0.001$ for both lines).

These findings underscore the relative drug resistance of 3D clusteroids and emphasize the importance of cell model selection in evaluating redox-based therapies. Consistent with expectations, the oxidative combination of ATO and D-VC induced a greater cytotoxic effect in 2D monolayers compared to 3D CRC cell cultures. In both HCT116 and SW620 cell lines, clusteroids exhibited minimal responsiveness, likely due to the presence of the ECM, which serves as a physical barrier that restricts drug access to inner cell layers.[26–28]

In 2D cell monolayers, treatment with ATO, D-VC, and their combination produced responses consistent with previous studies,[2,24] confirming a pronounced synergistic effect relative to monotherapies. We observed stronger suppression of cell proliferation and viability under 2D conditions, while the effect in the 3D culture model remained weak. The data presented in Fig. 6 and 7 demonstrate that our specific nano-formulation, comprising 0.6 wt% Sav-coated ATO/D-VC loaded shellac NPs sterically stabilised by 0.05 wt% Poloxamer 407, showed substantial enhancement in anticancer efficacy within 3D CRC tumour clusteroid models. The nanocarrier surface coated with Savinase led to partial digestion of the ECM of the 3D

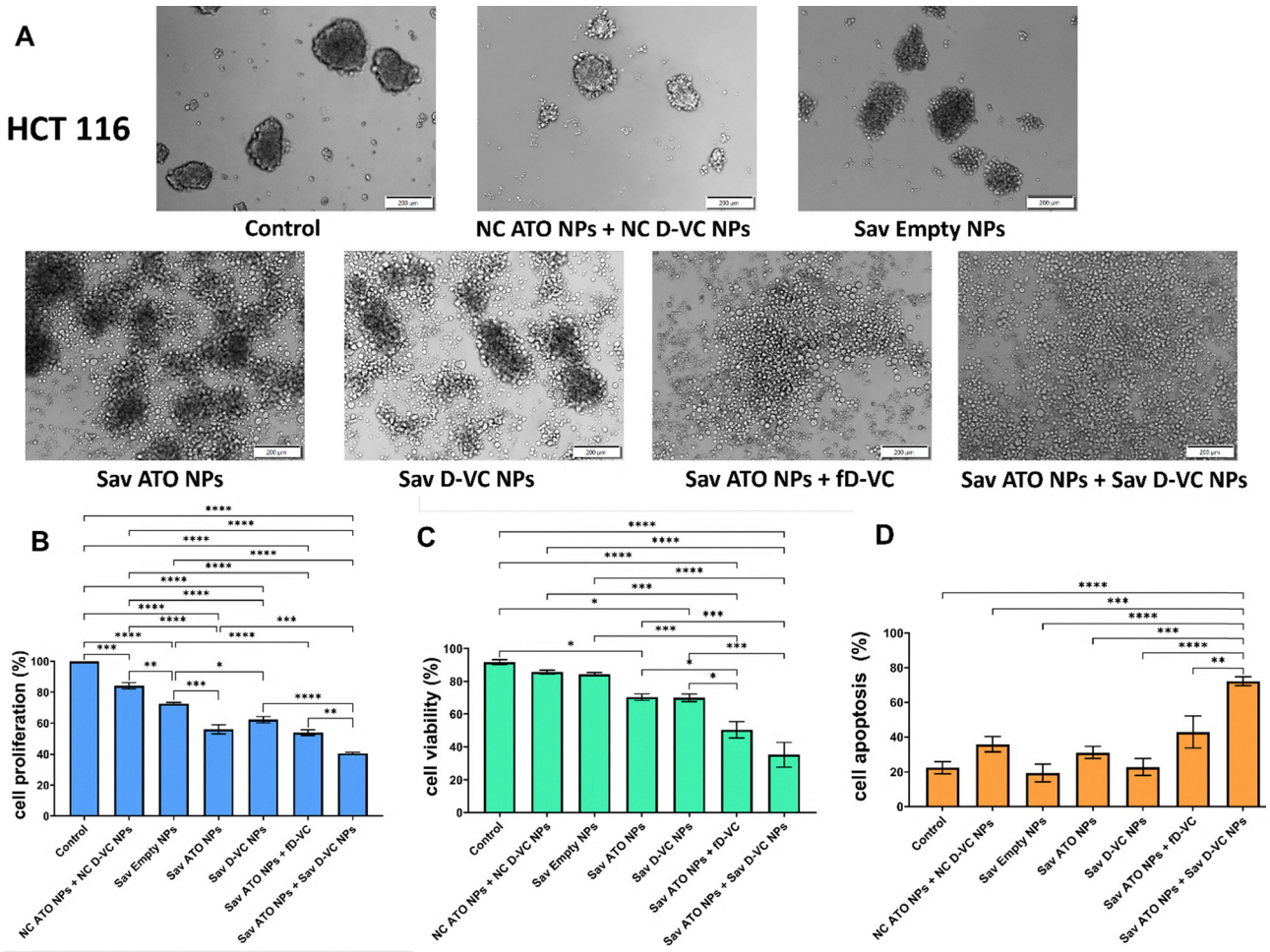

Fig. 6 Effect of Savinase-coated ATO/D-VC loaded NPs formulations on HCT116 clusteroids. (A) Representative brightfield images of HCT116 clusteroids following 48-h treatment with ATO (7.5 μM) and D-VC (1.5 mM) delivered in Sav-NP formulations: untreated control, Savinase-coated empty nanoparticles (Sav-NPs), Savinase-coated nanoparticles loaded with ATO (Sav-ATO NPs), Savinase-coated nanoparticles loaded with D-VC (Sav-D-VC NPs), Sav-ATO NPs combined with free D-VC, and combined treatment with both Sav-ATO NPs and Sav-D-VC NPs. Scale bars: 200 μm. (B) Quantitative analysis of cell proliferation in clusteroids after treatment, measured by MTS assay and expressed relative to untreated controls. (C) Cell viability was assessed by Hoechst/PI staining, presented as the percentage of viable cells for each treatment group. (D) Apoptosis assay performed by flow cytometry using Annexin V and PI staining. The percentage of early and late apoptotic cells (Annexin V-positive cells) is shown for each treatment group, revealing increased apoptosis in response to drug-loaded NPs treatments, especially in combination groups. All quantitative data are shown as mean ± standard deviation (SD) from at least three independent biological replicates.

structures,[42,48–52] which increased the clusteroid porosity and the nanocarrier penetration in the clusteroids cores (Fig. 6(A) and 7(A) for HCT116 and SW620).

Loading of ATO and D-VC into Sav-NPs made of shellac–poloxamer significantly enhanced cytotoxic outcomes in 3D cell cultures compared to both free drug combinations and uncoated nanoparticle formulations. Encapsulating the oxidative drugs in shellac–poloxamer NPs protects them from premature degradation, allows sustained release, and increases the drug concentration reaching the tumour.[44] This improvement in therapeutic effect appears to result from a combination of enzymatic interaction with the clusteroid microenvironment and favourable electrostatic adhesion conferred by the Savinase coating. The morphological changes observed in brightfield images, particularly the dissociation of clusteroids in the Sav-ATO and Sav-D-VC NP groups, suggest that the presence of the Savinase coating contributed to partial disintegration of the clusteroid structure (Fig. 6(A) and 7(A)). Using Savinase as a surface coating facilitates localized digestion of the ECM, hence improving nanoparticle access to deeper cell layers in the clusteroid cores.

This interpretation parallels prior reports involving lysozyme- and alcalase-coated nanoparticles, which enhanced penetration through dense biological matrices such as biofilms and cell spheroids.[38,46] Additionally, the cationic nature of the coating with Savinase, confirmed through zeta potential analysis (Fig. 1(G)), likely enhances nanoparticle deposition on the negatively charged cancer cell membranes. This electrostatic interaction may improve both surface retention and internalization.

These results demonstrate the importance of incorporating 3D cell model testing when evaluating therapeutic efficacy, particularly for solid tumour–targeted interventions. The

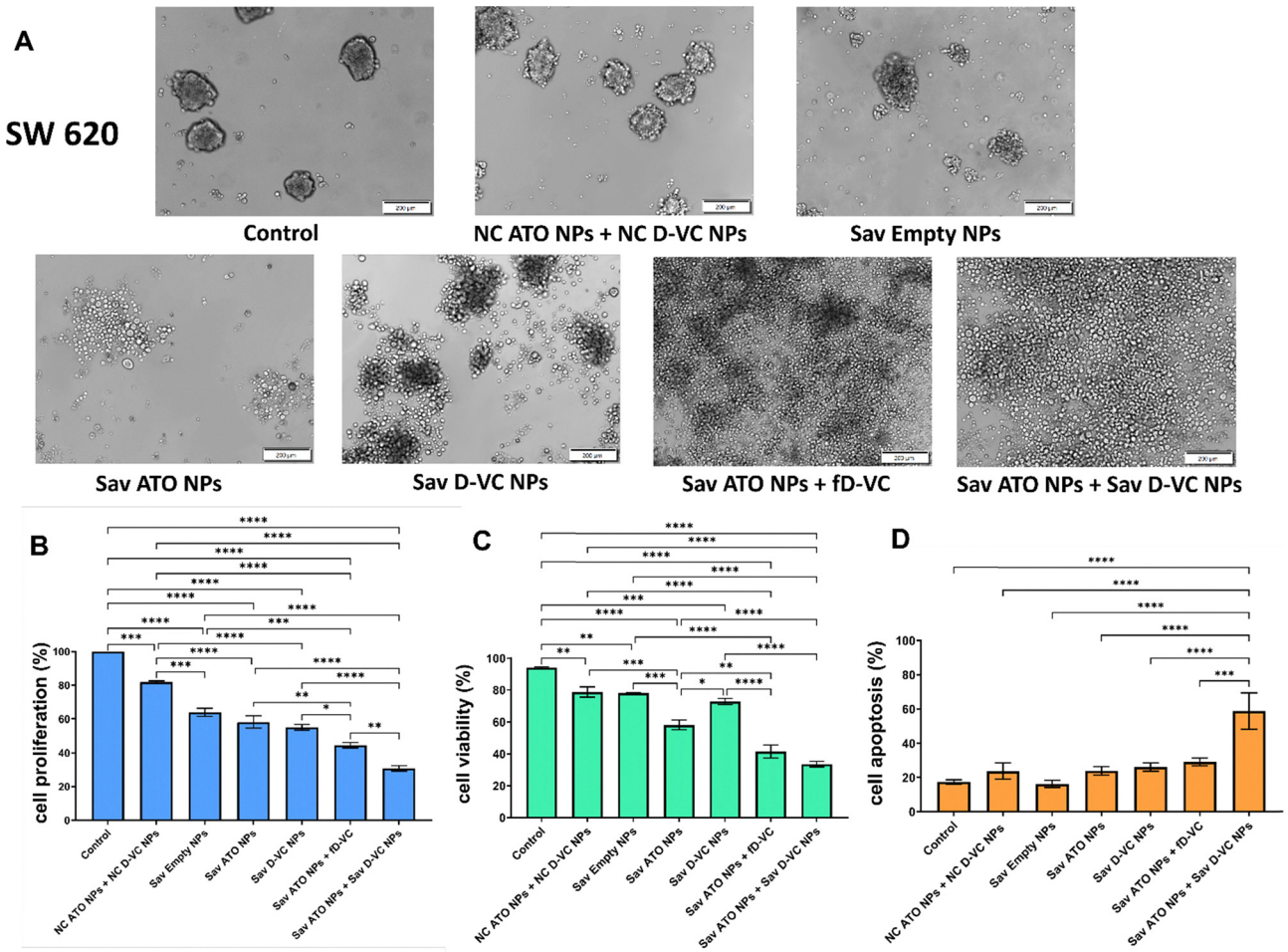

Fig. 7 Effect of Savinase-coated nanoparticle formulations on SW620 clusteroids. (A) Representative brightfield images of SW620 clusteroids following 48-hour treatment with ATO (7.5 μM) and D-VC (1.5 mM) delivered in Sav nanoparticle formulations: untreated control, Savinase-coated empty nanoparticles (Sav-NPs), Savinase-coated nanoparticles loaded with ATO (Sav-ATO NPs), Savinase-coated nanoparticles loaded with D-VC (Sav-D-VC NPs), Sav-ATO NPs combined with free D-VC, and combined treatment with both Sav-ATO NPs and Sav-D-VC NPs. Scale bars: 200 μm. (B) Quantitative analysis of cell proliferation in clusteroids after treatment, measured by MTS assay and expressed relative to untreated controls. (C) Cell viability assessed by Hoechst/PI staining, presented as the percentage of viable cells for each treatment group. (D) Apoptosis assay performed by flow cytometry using Annexin V and PI staining. The percentage of early and late apoptotic cells (Annexin V-positive cells) is shown for each treatment group, revealing increased apoptosis in response to drug-loaded nanoparticle treatments, especially in combination groups. All quantitative data are shown as mean ± standard deviation (SD) from at least three independent biological replicates.

observed trend is consistent with previous findings in cell spheroid systems derived from breast and pancreatic cancers, where limited drug diffusion has similarly led to underestimation of treatment effectiveness in traditional 2D assays.[28] These parallels further validate the clusteroid model as a physiologically relevant platform for analysing drug resistance capability. It is important to note that the reduced susceptibility of clusteroids does not indicate treatment failure but rather reflects the limitations of single-dose exposure. In clinical and preclinical studies of tumour therapy, repeated dosing is commonly employed to achieve sustained therapeutic effects. Encapsulation of the drug in an active nanocarrier may help address this limitation by enhancing local bioavailability and reducing the frequency and duration of treatment. Together, these findings highlight the importance of the dimensional context on drug efficacy and support the growing implementation of 3D models in preclinical testing.

While the presence of Savinase coating on the nanocarriers clearly has a loosening effect, as seen in Fig. 6(A) for HCT116 and Fig. 7(B) for SW620, the cell viability, proliferation and apoptosis assessment shows a more moderate effect (Fig. 6(B)–(D) and 7(B)–(D)). This can be partially explained by the timescale of the release of more than 80% of both ATO and D-VC from the Sav-NPs, which occurs over a period of 10–12 h compared with the period of the treatment, which is 48 h. Therefore, before the full loosening up of the ECM of the 3D cell culture, the nanocarriers get exhausted from their ATO and D-VC payloads, which have diffused out in the media. Hence, the nanocarrier drug delivery effect has a shorter period of action than the enzymatic action of its coating. Since in clinical practice repetitive doses of ATO are given to the patients (chemo is given in courses), this opens the possibility to do additional treatment of the tumor with Sav-coated ATO/D-VC NPs which would further enhance the therapy.

A crucial aspect of this study is the role of oxidative stress in the cytotoxic mechanism of ATO and D-VC. Both agents independently increase intracellular reactive oxygen species (ROS) levels, but their combination leads to a heightened oxidative burden that cancer cells cannot counteract, resulting in suicidal ROS production by mitochondria (SMRP) and subsequent apoptosis.[2,22,24] In addition to ROS-mediated cytotoxicity, ATO disrupts the glutathione antioxidant system and key oncogenic signalling pathways, such as PI3K/AKT/mTOR, that sustain KRAS-mutant CRC survival and proliferation.[13–15,22] D-VC further enhances this effect by impairing mitochondrial ATP production, weakening the metabolic adaptability of cancer cells. These mechanisms collectively contribute to the increased efficacy of the ATO-D-VC combination in targeting treatment-resistant CRC.

To provide insights into the mechanisms underlying the anticancer activity of ATO and D-VC, we examined the effects of ATO and D-VC NPs on the oxidative stress modulation and mitochondrial dysfunction in 3D CRC cultures using MitoSOX and MitoTracker Green/Deep Red. A combination of Sav-coated ATO loaded and Sav-coated D-VC loaded NPs led to a significant increase in the percentage of MitoSox-positive cells, indicating robust ROS production (Fig. 8(A) and (B)). This was accompanied by a marked decrease in the proportion of cells with high

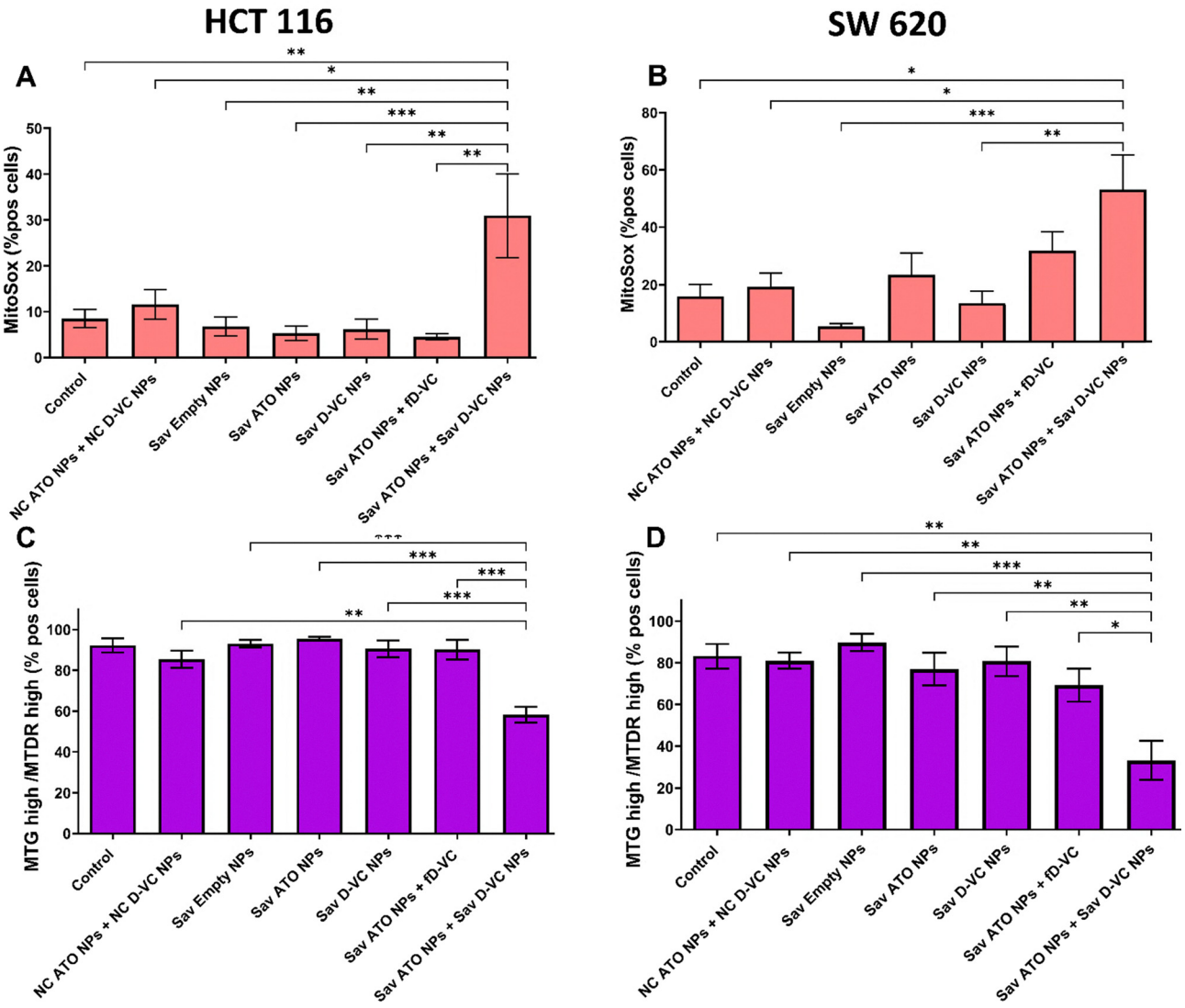

Fig. 8 Assessment of mitochondrial function upon nanoparticle treatment. (A) Measurement of mitochondrial reactive oxygen species (ROS) production using flow cytometry and MitoSOX Red staining in HCT116 and (B) in SW620 cells. The percentage of MitoSOX-positive cells is shown for each treatment group, demonstrating increased ROS generation upon exposure to the combination treatment of Sav NPs loaded with ATO and D-VC, with the combination inducing the highest ROS levels in 3D clusteroids. (C) Analysis of mitochondrial function in treated HCT116 3D cultures, assessed by the proportion of cells double positive for MitoTracker Green (MTG, total mitochondria) and MitoTracker Deep Red (MTDR, polarized mitochondria). The percentage of MTG+/MTDR+ cells reflects the maintenance of functional mitochondria under each condition, with a marked decrease observed following the combination treatment with Sav ATO and Sav D-VC NPs, indicating mitochondrial dysfunction. (D) The same in the SW620 cell line. All quantitative data are shown as mean ± standard deviation (SD) from at least three independent biological replicates.

MTG/MTDR signals, reflecting mitochondrial depolarization and dysfunction (Fig. 8(C) and (D)). Additional flow cytometry data for the cell apoptosis following treatments with ATO and D-VC encapsulated in Sav-coated NPs with positive and negative controls for 3D HCT116 and 3D SW620 are available in Fig. S6 and S7 (SI). The enhanced performance of Savinase-functionalized nanoparticles across both colorectal cancer models highlights the therapeutic benefit of delivering ATO and D-VC as encapsulated in a protease surface-functionalized NP formulation. The combined application of Sav-ATO and Sav-D-VC nanoparticles yielded the most pronounced treatment response, consistent with the proposed mechanism involving improved penetration and surface targeting within 3D clusteroids. This outcome, supported by cell viability and proliferation assays, reinforces the importance of combining enzymatic surface activity with dual-agent delivery to address the diffusion barriers characteristic of dense tumour-like structures. The observed benefits of Sav-NPs are consistent with broader trends in nano-oncology, which increasingly employ surface-modified nanocarriers to enhance barrier penetration across diverse applications, including tumour ECM, bacterial biofilms, and intracellular organelles.[30,38,46,53] Unlike mitochondria-targeted nanocarriers that depend on synthetic moieties such as triphenylphosphonium,[53] the Savinase-coated shellac–poloxamer system is based on biocompatible materials and incorporates a clinically used enzyme, supporting its translational potential. This aligns with emerging perspectives in the field that emphasize biocompatibility and functional versatility for future clinical applications.[44] An unexpected observation was the reduced cytotoxicity upon treatment with uncoated ATO/D-VC nanoparticles compared to the free-drug formulation at 48 h. This may be explained by incomplete or delayed release of encapsulated drugs from the shellac matrix, a phenomenon similarly noted in metformin-loaded lysozyme-coated particles under suboptimal coating conditions.[38] These results highlight a critical balance between nanoparticle stability and drug release kinetics: excessive matrix integrity can hinder timely drug availability, while insufficient stability may reduce retention at the target site.

The increased selectivity of this approach stems from the differential oxidative stress tolerance between cancerous and normal cells, allowing for targeted cell death with minimal damage to healthy tissues. Given the structural complexity and ECM barriers present in 3D CRC cell culture models, the free ATO and D-VC combination exhibited reduced cytotoxicity compared to 2D cultures. Moreover, a modest increase in ROS levels was observed in 3D clusteroid models, suggesting differential redox sensitivity in spatially structured models in comparison with monolayer cultures. It is likely that the treatment with free drugs or NPs loaded without coating primarily affects cells at the periphery of the clusteroids, with limited impact on cells deeper within the core. Our previous studies have shown that while both L-VC and D-VC induce oxidative stress, D-VC demonstrates similar effectiveness and lower toxicity in animal models, making it a promising candidate for further clinical translation.[23]

Conclusions

Although the ATO and D-VC drug combination has shown strong efficacy in 2D cancer cell cultures, animal models, and early clinical trials, insight into its behaviour in systems that closely replicate the structural features of the tumour microenvironment remains limited. Therefore, 3D *in vitro* models offer a valuable platform for bridging this gap. This study evaluated the cytotoxicity of ATO and D-VC in 3D cell models known as clusteroids, derived from two KRAS-mutant CRC cell lines, HCT116 and SW620, and directly compared their response to corresponding 2D cultures. Clusteroids closely mimic key aspects of the tumour environment, including cell–cell interactions, ECM deposition, and limited drug diffusion, offering a more predictive platform for assessing treatment efficacy. While ATO/D-VC showed a synergistic cytotoxic effect in the 2D culture, the response in 3D clusteroids was significantly reduced, suggesting that drug access to inner cell layers was limited by ECM barriers. To improve the drug delivery, ATO and D-VC were individually encapsulated in shellac–poloxamer nanoparticles functionalized with Savinase, a protease known to degrade ECM components. These nanoparticles exhibited good colloidal stability, a positive surface charge to enhance interaction with negatively charged cancer cells, and enzymatic activity to access cells in the core of the 3D cell models. In clusteroids, co-delivery of the two nanoparticle formulations restored and enhanced the cytotoxic effect of ATO/D-VC, outperforming both free drug and uncoated formulations. This dual-nanoparticle approach preserved the synergistic interaction and led to a substantial reduction in viability and proliferation, particularly in CRC cells. These results highlight the importance of 3D models in preclinical evaluation and demonstrate the potential of functionalized nanoparticles to enhance oxidative drug delivery in solid tumours. Such Sav-coated nanocarriers of ATO and D-VC are not intended for intravenous delivery due to potential immunogenic response. A potentially suitable way of administration in animal models may involve direct injection of the Sav-NP suspension into the solid tumour.

Future perspectives

Following the promising *in vitro* results presented here, future work will focus on *in vivo* evaluation of Sav-NP pharmacokinetics, biodistribution, tumour penetration, and therapeutic efficacy using animal models of colorectal cancer. Further refinement of the nanoparticle system will include optimizing Savinase coating levels, adjusting shellac crosslinking to balance particle stability with controlled drug release, and refining ATO and D-VC concentrations based on molybdate assay of ATO and dialysis data. Combining real-time release profiles with ECM profiling and *in vivo* outcomes will support the development of more effective and clinically relevant nanoparticle formulations in the future.

Overall, ATO and D-VC function as potent oxidative stress modulators, capable of inducing selective cytotoxicity

in colorectal cancer. This study demonstrates the therapeutic potential of combining these two oxidative drugs with ECM-digesting, positively charged nanocarriers for improved treatment of colorectal cancer. Savinase-functionalized nanoparticles successfully enhanced the cytotoxic activity of ATO and D-VC in the 3D cell culture, exceeding the efficacy of both free drugs and uncoated nanoparticle formulations. This drug delivery method represents a promising approach for overcoming therapeutic resistance and deserves further investigation in preclinical and clinical settings. This synergistic approach addresses critical challenges in drug delivery, also beyond ATO and D-VC, offering a more effective and safer platform for cancer therapy. By placing these findings in the broader context of oxidative therapies,[2,24] 3D tumour modelling,[26–28,30] and protease-coated nanomedicines,[38,46] the current work contributes to the advancement of clinically applicable nanoformulations for solid tumour therapy.

Author contributions

The manuscript was written through the contributions of all authors. All authors have given approval to the final version of the manuscript.

Conflicts of interest

There are no conflicts to declare.

Data availability

All data supporting this research article are incorporated as part of the supporting information (SI) file and the main text. Supporting information: the following are additional data: (i) Fig. S1A: absorbance at 880 nm of the reaction mixture *versus* the ATO concentration as a calibration plot for quantification of free ATO in solution; (ii) Fig. S1B: absorbance at 520 nm of the DCPIP/D-VC reaction mixture *versus* the D-VC concentration as a calibration plot for quantification of free D-VC in solution; (iii) Fig. S1C: D-VC released *versus* time; (iv) Fig. S2: (A) effect of the ATPS Dex-in-PEO emulsion formation technique on the clusteroid morphology, and (B) effect of the culture plate coating on the growth of the clusteroids; (v) Fig. S3: uniformity of clusteroid size across conditions prior to treatment; (vi) Fig. S4: size distribution of HCT116 clusteroids before and after 48-hour treatment with oxidative drug combinations; (vii) Fig. S5: size distribution of SW620 clusteroids before and after 48-hour treatment with oxidative drug combinations; (viii) Fig. S6: flow cytometry analysis of apoptosis in 3D HCT116 clusteroids using Annexin V and propidium iodide (PI) staining; and (ix) Fig. S7: flow cytometry analysis of apoptosis in 3D SW620 clusteroids using Annexin V and propidium iodide (PI) staining. See DOI: **https://doi.org/10.1039/d5tb01882j**.

Acknowledgements

This research was funded by the Committee of Science of the Ministry of Science and Higher Education of the Republic of Kazakhstan (grant no. AP19677474, Principal Investigator: A. N. B.). Authors are also grateful to Dr A. Wang from University of Macao (PRC) for useful advice about 3D cell culture.

References

1 W. Tian, Z. Wang, N.-N. Tang, J.-T. Li, Y. Liu, W.-F. Chu and B.-F. Yang, Ascorbic Acid Sensitizes Colorectal Carcinoma to the Cytotoxicity of Arsenic Trioxide *via* Promoting Reactive Oxygen Species-Dependent Apoptosis and Pyroptosis, *Front. Pharmacol.*, 2020, **11**, 123, DOI: **10.3389/fphar.2020.00123**.

2 X. Wu, M. Park, D. A. Sarbassova, H. Ying, M. G. Lee, R. Bhattacharya, L. Ellis, C. B. Peterson, M. C. Hung and H. K. Lin, A chirality-dependent action of vitamin C in suppressing Kirsten rat sarcoma mutant tumor growth by the oxidative combination: Rationale for cancer therapeutics, *Int. J. Cancer*, 2020, **146**, 2822–2828, DOI: **10.1002/ijc.32658**.

3 N. I. Noguera, E. Pelosi, D. F. Angelini, M. Liliana Piredda, G. Guerrera, E. Piras, L. Battistini, L. Massai, A. Berardi, G. Catalano, L. Cicconi, G. Castelli, A. D'Angiò, L. Pasquini, G. Graziani, G. Fioritoni, M. Teresa Voso, D. Mastrangelo, U. Testa and F. Lo-Coco, High-dose ascorbate and arsenic trioxide selectively kill acute myeloid leukemia and acute promyelocytic leukemia blasts *in vitro*, *Oncotarget*, 2017, **8**, 32550–32565, DOI: **10.18632/oncotarget.15925**.

4 L. Jiang, L. Wang, L. Chen, G.-H. Cai, Q.-Y. Ren, J.-Z. Chen, H.-J. Shi and Y.-H. Xie, As_2O_3 induces apoptosis in human hepatocellular carcinoma HepG2 cells through a ROS-mediated mitochondrial pathway and activation of caspases, *Int. J. Clin. Exp. Med.*, 2015, **8**, 2190. PMID: 25932150; PMCID: PMC4402797.

5 X. Li, D. Xianzhong and T. E. Adrian, Arsenic Trioxide Causes Redistribution of Cell Cycle, Caspase Activation, and GADD Expression in Human Colonic, Breast, and Pancreatic Cancer Cells, *Cancer Invest.*, 2004, **22**, 389–400, DOI: **10.1081/CNV-200029068**.

6 A. M. Walker, J. J. Stevens, K. Ndebele and P. B. Tchounwou, Arsenic trioxide modulates DNA synthesis and apoptosis in lung carcinoma cells, *Int. J. Environ. Res. Public Health*, 2010, **7**, 1996–2007, DOI: **10.3390/ijerph7051996**.

7 G. Nauman, J. C. Gray, R. Parkinson, M. Levine and C. J. Paller, Systematic Review of Intravenous Ascorbate in Cancer Clinical Trials, *Antioxidants*, 2018, **7**, 89, DOI: **10.3390/antiox7070089**.

8 W. Tian, Z. Wang, N.-N. Tang, J.-T. Li, Y. Liu, W.-F. Chu and B.-F. Yang, Ascorbic Acid Sensitizes Colorectal Carcinoma to the Cytotoxicity of Arsenic Trioxide *via* Promoting Reactive Oxygen Species-Dependent Apoptosis and Pyroptosis, *Front. Pharmacol.*, 2020, **11**, 123, DOI: **10.3389/fphar.2020.00123**.

9 S. Kumar, C. G. Yedjou and P. B. Tchounwou, Arsenic trioxide induces oxidative stress, DNA damage, and mitochondrial pathway of apoptosis in human leukemia (HL-60) cells, *J. Exp. Clin. Cancer Res.*, 2014, **33**, 42, DOI: **10.1186/1756-9966-33-42**.

10 M. Dawood, S. Hamdoun and T. Efferth, Multifactorial Modes of Action of Arsenic Trioxide in Cancer Cells as Analyzed by Classical and Network Pharmacology, *Front. Pharmacol.*, 2018, **9**, 143, DOI: **10.3389/fphar.2018.00143**.

11 D. Mastrangelo, E. Pelosi, G. Castelli, F. Lo-Coco and U. Testa, Mechanisms of anti-cancer effects of ascorbate: Cytotoxic activity and epigenetic modulation, *Blood Cells, Mol., Dis.*, 2018, **69**, 57–64, DOI: **10.1016/j.bcmd.2017.09.005**.

12 S. J. Padayatty, H. Sun, Y. Wang, H. D. Riordan, S. M. Hewitt, A. Katz, R. A. Wesley and M. Levine, Vitamin C Pharmacokinetics: Implications for Oral and Intravenous Use, *Ann. Intern. Med.*, 2004, **140**, 533–537, DOI: **10.7326/0003-4819-140-7-200404060-00010**.

13 Q. Chen, M. G. Espey, A. Y. Sun, J. H. Lee, M. C. Krishna, E. Shacter, P. L. Choyke, C. Pooput, K. L. Kirk, G. R. Buettner and M. Levine, Ascorbate in pharmacologic concentrations selectively generates ascorbate radical and hydrogen peroxide in extracellular fluid *in vivo*, *Proc. Natl. Acad. Sci. U. S. A.*, 2007, **104**, 8749–8754, DOI: **10.1073/pnas.0702854104**.

14 Q. Chen, M. G. Espey, A. Y. Sun, C. Pooput, K. L. Kirk, M. C. Krishna, D. B. Khosh, J. Drisko and M. Levine, Pharmacologic doses of ascorbate act as a prooxidant and decrease growth of aggressive tumor xenografts in mice, *Proc. Natl. Acad. Sci. U. S. A.*, 2008, **105**, 11105–11109, DOI: **10.1073/pnas.0804226105**.

15 M.-W. Baek, H.-S. Cho, S.-H. Kim, W.-J. Kim and J.-Y. Jung, Ascorbic Acid Induces Necrosis in Human Laryngeal Squamous Cell Carcinoma *via* ROS, PKC, and Calcium Signaling, *J. Cell. Physiol.*, 2017, **232**, 417–425, DOI: **10.1002/jcp.25438**.

16 Y. Takemura, M. Satoh, K. Satoh, H. Hamada, Y. Sekido and S. Kubota, High dose of ascorbic acid induces cell death in mesothelioma cells, *Biochem. Biophys. Res. Commun.*, 2010, **394**, 249–253, DOI: **10.1016/j.bbrc.2010.02.012**.

17 D. Fan, X. Liu, Z. Shen, P. Wu, L. Zhong and F. Lin, Cell signaling pathways based on vitamin C and their application in cancer therapy, *Biomed. Pharmacother.*, 2023, **162**, 114695, DOI: **10.1016/j.biopha.2023.114695**.

18 V. Camarena and G. Wang, The epigenetic role of vitamin C in health and disease, *Cell. Mol. Life Sci.*, 2016, **73**, 1645–1658, DOI: **10.1007/s00018-016-2145-x**.

19 G. N. Y. van Gorkom, R. G. J. Klein Wolterink, C. Van Elssen, L. Wieten, W. T. V. Germeraad and G. M. J. Bos, Influence of Vitamin C on Lymphocytes: An Overview, *Antioxidants*, 2018, **7**, 41, DOI: **10.3390/antiox7030041**.

20 L. H. Zeng, Q. M. Wang, L. Y. Feng, Y. D. Ke, Q. Z. Xu, A. Y. Wei, C. Zhang and R. B. Ying, High-dose vitamin C suppresses the invasion and metastasis of breast cancer cells *via* inhibiting epithelial-mesenchymal transition, *OncoTargets Ther.*, 2019, **12**, 7405–7413, DOI: **10.2147/ott.s222702**.

21 H. Sasaki, M. Shitara, K. Yokota, Y. Hikosaka, S. Moriyama, M. Yano and Y. Fujii, Overexpression of GLUT1 correlates with Kras mutations in lung carcinomas, *Mol. Med. Rep.*, 2012, **5**, 599–602, DOI: **10.3892/mmr.2011.736**.

22 A. N. Burska, B. Ilyassova, A. Dildabek, M. Khamijan, D. Begimbetova, F. Molnár and D. D. Sarbassov, Enhancing an Oxidative "Trojan Horse" Action of Vitamin C with Arsenic Trioxide for Effective Suppression of KRAS-Mutant Cancers: A Promising Path at the Bedside, *Cells*, 2022, **11**, 3454, DOI: **10.3390/cells11213454**.

23 D. Begimbetova, A. N. Burska, A. Baltabekova, A. Kussainova, A. Kukanova, F. Fazyl, M. Ibragimova, K. Manekenova, A. Makishev, R. I. Bersimbaev and D. D. Sarbassov, The Vitamin C Enantiomers Possess a Comparable Potency in the Induction of Oxidative Stress in Cancer Cells but Differ in Their Toxicity, *Int. J. Mol. Sci.*, 2024, **25**, 2531, DOI: **10.3390/ijms25052531**.

24 D. Begimbetova, A. Kukanova, F. Fazyl, K. Manekenova, T. Omarov, A. N. Burska, M. Khamijan, A. Gulyayev, B. Yermekbayeva, A. Makishev, T. Saliev, K. Batyrbekov, C. Aitbayev, Z. Spatayev and D. Sarbassov, The Oxidative Drug Combination for Suppressing KRAS G12D Inducible Tumour Growth, *BioMed Res. Int.*, 2022, **2022**, 9426623, DOI: **10.1155/2022/9426623**.

25 A. S. Pires, C. R. Marques, J. C. Encarnação, A. M. Abrantes, I. A. Marques, M. Laranjo, R. Oliveira, J. E. Casalta-Lopes, A. C. Gonçalves, A. B. Sarmento-Ribeiro and M. F. Botelho, Ascorbic Acid Chemosensitizes Colorectal Cancer Cells and Synergistically Inhibits Tumor Growth, *Front. Physiol.*, 2018, **9**, 911, DOI: **10.3389/fphys.2018.00911**.

26 A. Wang, L. A. Madden and V. N. Paunov, Advanced biomedical applications based on emerging 3D cell culturing platforms, *J. Mater. Chem. B*, 2020, **8**, 10487–10501, DOI: **10.1039/D0TB01658F**.

27 W. H. Abuwatfa, W. G. Pitt and G. A. Husseini, Scaffold-based 3D cell culture models in cancer research, *J. Biomed. Sci.*, 2024, **31**, 7, DOI: **10.1186/s12929-024-00994-y**.

28 L. C. Kimlin, G. Casagrande and V. M. Virador, *In vitro* three-dimensional (3D) models in cancer research: an update, *Mol. Carcinog.*, 2013, **52**, 167–182, DOI: **10.1002/mc.21844**.

29 A. K. F. Dyab, A. N. Burska and V. N. Paunov, Aqueous two-phase emulsion systems in 3D cell culture, *Curr. Opin. Colloid Interface Sci.*, 2025, **78**, 101933, DOI: **10.1016/j.cocis.2025.101933**.

30 A. Wang, P. J. Weldrick, L. A. Madden and V. N. Paunov, Biofilm-Infected Human Clusteroid Three-Dimensional Coculture Platform to Replace Animal Models in Testing Antimicrobial Nanotechnologies, *ACS Appl. Mater. Interfaces*, 2021, **13**, 22182–22194, DOI: **10.1021/acsami.1c02679**.

31 A. Wang, L. A. Madden and V. N. Paunov, Fabrication of Angiogenic Sprouting Coculture of Cell Clusteroids Using an Aqueous Two-Phase Pickering Emulsion System, *ACS Appl. Bio Mater.*, 2022, **5**, 1804–1816, DOI: **10.1021/acsabm.2c00168**.

32 V. P. Vineetha and K. G. Raghu, An Overview on Arsenic Trioxide-Induced Cardiotoxicity, *Cardiovasc. Toxicol.*, 2019, **19**, 105–119, DOI: **10.1007/s12012-018-09504-7**.

33 J. Wen, A. Li, Z. Wang, X. Guo, G. Zhang, M. R. Litzow and Q. Liu, Hepatotoxicity induced by arsenic trioxide: clinical features, mechanisms, preventive and potential therapeutic strategies, *Front. Pharmacol.*, 2025, **16**, 1536388, DOI: **10.3389/fphar.2025.1536388**.

34 S.-F. Yip, Y.-M. Yeung and E.-Y.-K. Tsui, Severe neurotoxicity following arsenic therapy for acute promyelocytic leukemia: potentiation by thiamine deficiency, *Blood*, 2002, **99**, 3481–3482, DOI: 10.1182/blood-2001-12-0325.

35 Y. Li, J. Shi, S. Yu, X. Lu, Y. Li, W. Zheng, X. Zhang, W. Du, C. Zhao, L. Huang, X. Zhu, M. Li, L. Wang, J. Guo, H. Feng, Y. Gao and Z. Yu, Nanodelivery of arsenic trioxide induces macrophage-governed cGAS-STING signaling to remodel immune microenvironment in hepatocellular carcinoma, *Chem. Eng. J.*, 2025, **506**, 159943, DOI: 10.1016/j.cej.2025.159943.

36 A. Akhtar, S. X. Wang, L. Ghali, C. Bell and X. Wen, Recent advances in arsenic trioxide encapsulated nanoparticles as drug delivery agents to solid cancers, *J. Biomed. Res.*, 2017, **31**, 177, DOI: 10.7555/JBR.31.20160059.

37 M. Sönksen, K. Kerl and H. Bunzen, Current status and future prospects of nanomedicine for arsenic trioxide delivery to solid tumors, *Med. Res. Rev.*, 2022, **42**, 374–398, DOI: 10.1002/med.21844.

38 A. Wang, L. A. Madden and V. N. Paunov, Enhanced anticancer effect of lysozyme-functionalized metformin-loaded shellac nanoparticles on a 3D cell model: role of the nanoparticle and payload concentrations, *Biomater. Sci.*, 2024, **12**, 4735–4746, DOI: 10.1039/d4bm00692e.

39 J. Liu, H. Yu, J. Kong, X. Ge, Y. Sun, M. Mao, D. Y. Wang and Y. Wang, Preparation, characterization, stability, and controlled release of chitosan-coated zein/shellac nanoparticles for the delivery of quercetin, *Food Chem.*, 2024, **444**, 138634, DOI: 10.1016/j.foodchem.2024.138634.

40 K. Ma, Y. Qiu, Y. Fu and Q.-Q. Ni, Improved shellac mediated nanoscale application drug release effect in a gastric-site drug delivery system, *RSC Adv.*, 2017, **7**, 53401–53406, DOI: 10.1039/C7RA10757A.

41 Y. Yuan, S. Zhang, M. Ma, Y. Xu and D. Wang, Delivery of curcumin by shellac encapsulation: Stability, bioaccessibility, freeze-dried redispersibility, and solubilization, *Food Chem.: X*, 2022, **15**, 100431, DOI: 10.1016/j.fochx.2022.100431.

42 A. Wang, L. A. Madden and V. N. Paunov, High-throughput fabrication of hepatic cell clusteroids with enhanced growth and functionality for tissue engineering applications, *Mater. Adv.*, 2020, **1**, 3022–3032, DOI: 10.1039/D0MA00635A.

43 A. Wang, L. A. Madden and V. N. Paunov, Vascularized Co-Culture Clusteroids of Primary Endothelial and Hep-G2 Cells Based on Aqueous Two-Phase Pickering Emulsions, *Bioengineering*, 2022, **9**, 126, DOI: 10.3390/bioengineering9030126.

44 E. Karahmet Sher, M. Alebić, M. Marković Boras, E. Boškailo, E. Karahmet Farhat, A. Karahmet, B. Pavlović, F. Sher and L. Lekić, Nanotechnology in medicine revolutionizing drug delivery for cancer and viral infection treatments, *Int. J. Pharm.*, 2024, **660**, 124345, DOI: 10.1016/j.ijpharm.2024.124345.

45 M. Zhu, P. Wang, B. Chen, L. Shi, R. Long, S. Wang and Y. Liu, Active-oxygenating hollow Prussian blue nanosystems loaded with biomacromolecules for photodynamic/photothermal therapy of cancer and alleviating hypoxic tumors, *Mater. Des.*, 2024, **237**, 112618, DOI: 10.1016/j.matdes.2023.112618.

46 A. Wang, P. J. Weldrick, L. A. Madden and V. N. Paunov, Enhanced clearing of Candida biofilms on a 3D urothelial cell *in vitro* model using lysozyme-functionalized fluconazole-loaded shellac nanoparticles, *Biomater. Sci.*, 2021, **9**, 6927–6939, DOI: 10.1039/d1bm01035b.

47 O. Urzì, R. Gasparro, E. Costanzo, A. De Luca, G. Giavaresi, S. Fontana and R. Alessandro, Three-Dimensional Cell Cultures: The Bridge between *In Vitro* and *In Vivo* Models, *Int. J. Mol. Sci.*, 2023, **24**, 12046, DOI: 10.3390/ijms241512046.

48 S. B. G. Celik, S. R. Dominici, B. W. Filby, A. A. K. Das, L. A. Madden and V. N. Paunov, Fabrication of Human Keratinocyte Cell Clusters for Skin Graft Applications by Templating Water-in-Water Pickering Emulsions, *Biomimetics*, 2019, **4**, 50, DOI: 10.3390/biomimetics4030050.

49 A. A. K. Das, B. W. Filby, D. A. Geddes, D. Legrande and V. N. Paunov, High throughput fabrication of cell spheroids by templating water-in-water Pickering emulsions, *Mater. Horiz.*, 2017, **4**, 1196–1200, DOI: 10.1039/C7MH00677B.

50 C. Han, S. Takayama and J. Park, Formation and manipulation of cell spheroids using a density adjusted PEG/DEX aqueous two phase system, *Sci. Rep.*, 2015, **5**, 11891, DOI: 10.1038/srep11891.

51 A. Tevlek, S. Kecili, O. S. Ozcelik, H. Kulah and H. C. Tekin, Spheroid Engineering in Microfluidic Devices, *ACS Omega*, 2023, **8**, 3630–3649, DOI: 10.1021/acsomega.2c06052.

52 A. Cacciamali, R. Villa and S. Dotti, 3D Cell Cultures: Evolution of an Ancient Tool for New Applications, *Front. Physiol.*, 2022, **13**, 836480, DOI: 10.3389/fphys.2022.836480.

53 S. Mani, G. Swargiary, S. Tyagi, M. Singh, N. K. Jha and K. K. Singh, Nanotherapeutic approaches to target mitochondria in cancer, *Life Sci.*, 2021, **281**, 119773, DOI: 10.1016/j.lfs.2021.119773.

54 S. S. M. Al-Obaidy, G. M. Greenway, S. Kalmagambetova and V. N. Paunov, Dual surface functionalised curcumin-shellac nano-delivery system with enhanced antimicrobial action, *RSC Adv.*, 2025, **15**, 25497–25509, DOI: 10.1039/D5RA03212A.

55 P. J. Weldrick, M. J. Hardman and V. N. Paunov, Enhanced Clearing of Wound-Related Pathogenic Bacterial Biofilms Using Protease-Functionalized Antibiotic Nanocarriers, *ACS Appl. Mater. Interfaces*, 2019, **11**, 43902–43919, DOI: 10.1021/acsami.9b16119.

56 P. J. Weldrick, M. J. Hardman and V. N. Paunov, Smart active antibiotic nanocarriers with protease surface functionality can overcome biofilms of resistant bacteria, *Mater. Chem. Front.*, 2021, **5**, 961–972, DOI: 10.1039/D0QM00874E.

57 P. J. Weldrick, S. San and V. N. Paunov, Advanced Alcalase-Coated Clindamycin-Loaded Carbopol Nanogels for Removal of Persistent Bacterial Biofilms, *ACS Appl. Nano Mater.*, 2021, **4**, 1187–1201, DOI: 10.1021/acsanm.0c02810.

58 P. J. Weldrick, M. J. Hardman and V. N. Paunov, Super-Enhanced Removal of Fungal Biofilms by Protease-Functionalized Amphotericin B Nanocarriers, *Adv. Nanobiomed. Res.*, 2021, **1**, 2000027, DOI: 10.1002/anbr.202000027.

59 A. Wang, P. J. Weldrick, L. A. Madden and V. N. Paunov, Enhanced clearing of Candida biofilms on a 3D urothelial cell *in vitro* model using lysozyme-functionalized fluconazole-loaded shellac nanoparticles, *Biomater. Sci.*, 2021, **9**, 6927–6939, DOI: 10.1039/D1BM01035B.

